Robotics and Autonomous Systems 195 (2026) 105215

Contents lists available at ScienceDirect

Robotics and Autonomous Systems

journal homepage: www.elsevier.com/locate/robot

Dynamic model and performance assessment of the natural motion of a SCARA-like manipulator in pick-and-place tasks

Luca Bruzzone *, Matteo Verotti, Pietro Fanghella

Department of Mechanical, Energy Management and Transport Engineering (DIME), University of Genova, Via Opera Pia 15A, 16145 Genova (GE), Italy

ARTICLE INFO

Keywords:
Natural motion
Elastic balancing
Pick-and-place
Energy efficiency
SCARA

ABSTRACT

The energy efficiency of manipulators performing cyclic motions can be enhanced by utilizing the so-called natural motion, namely, the natural oscillations that occur when elastic elements are placed in series or parallel with the actuators. In this paper, the natural motion of the RR-4R-R robot is discussed. This manipulator exhibits a 4-DOF mobility similar to that of the widespread SCARA robot, but the vertical prismatic joint is replaced by a four-bar mechanism. This modification, along with the adoption of a direct-drive actuator for the four-bar mechanism, makes it easier to achieve the elastic balancing of the robot, allowing the exploitation of its natural motion. The robot dynamics is analysed using the Lagrangian approach. Two types of elastic balancing are considered: one using a torsional spring and one using a linear coil spring. A simplified model of the vertical motion is then proposed, decoupled from the inertial effects of the horizontal motion, and used to estimate the vertical natural period. The behaviour of the manipulator with natural elastic balancing is compared with that obtained with exact elastic balancing, which provides an indifferent equilibrium in any robot position. This comparison is first carried out in the time domain, and then the space of the robot operating conditions is sampled through multibody simulations, performed to investigate the threshold of convenience between exact and natural balancing. Simulation results indicate that exploiting the natural motion of the RR-4R-R manipulator can significantly reduce energy consumption in a wide range of industrial applications involving pick-and-place tasks.

1. Introduction

The improvement of energy efficiency in industrial plants plays a pivotal role in the global challenge of sustainability. In manufacturing, a significant portion of energy consumption is devoted to the handling of components and assemblies in robotized lines [1,2]. In these tasks, industrial robots usually waste most of their power on accelerating and decelerating their own mass in cyclic high-speed motions, rather than on moving their payload, especially in the case of serial robots, for which the ratio between payload mass and robot mass is low. Consequently, the investigation of energy-saving methods in robotics is becoming a fundamental research area. The International Federation of Robotics suggests sustainability and the reduction of energy consumption in robotic systems as one of the top global trends [3].

Energy-saving methods for robots can be divided into three categories: hardware, software, and mixed methods [4]. Hardware methods focus on the development of innovative physical architectures and components, such as lightweight manipulators [5–7], redundant actuation [8], and regenerative actuators and drivers [9,10]. Software methods focus on motion planning optimization to minimize energy consumption for a given set of task specifications [11–13]. Mixed approaches combine hardware and software aspects in a concurrent manner. Within this last category, a promising approach is the exploitation of the *natural motion*, or *free vibration response*, of a robotic manipulator equipped with elastic elements [14]. If a robot architecture includes elastic elements placed in series [15] or parallel [16] with the actuators, natural oscillations arise, which can be profitably exploited to perform cyclic motions if the robot and its motion are properly designed. In the theoretical case of friction absence, natural oscillations occur without energy consumption, due to the cyclic conversion between kinetic energy and elastic potential energy. However, real systems exhibit non-negligible friction, which causes the decrease of natural oscillations; nevertheless, cyclic motions close to the free vibration response can be maintained with limited energy consumption by the actuators, which compensate for the frictional losses.

In the last few years, several researchers have proposed different

* Corresponding author.
E-mail addresses: luca.bruzzone@unige.it (L. Bruzzone), matteo.verotti@unige.it (M. Verotti), pietro.fanghella@unige.it (P. Fanghella).

https://doi.org/10.1016/j.robot.2025.105215
Received 15 April 2025; Received in revised form 20 June 2025; Accepted 1 October 2025
Available online 3 October 2025

methods to tune the natural motion of the robot according to the task specifications (*natural elastic balancing*, [14]). The conceptually simplest methods are characterized by a predefined trajectory [17,18]: the robot motion, usually harmonic, is imposed, and the elastic elements are tuned to work close to resonance. With more complex approaches, both the elastic elements and the trajectory are concurrently optimized to match the free vibration response with the task requirements [19]. Another class of methods is based on trajectory learning, which involves acquiring the forced response at resonance and using it as a reference motion [20].

In this work, a predefined trajectory method is applied to the RR-4R-R manipulator [21]. Its mechanical architecture is similar to that of widely used SCARA robots (RRPR with vertical joint axes, Fig. 1, a). Still, the vertical prismatic joint, which is often actuated by a ball screw mechanism, is replaced with a four-bar parallelogram linkage that moves in a vertical plane. This design eliminates energy dissipation caused by prismatic joint friction. Moreover, the for-bar linkage can be actuated by a direct-drive actuator, reducing transmission friction losses. Finally, this configuration facilitates the integration of elastic elements (Fig. 1, b), enhancing the exploitation of the free vibration response [22].

SCARA robots are widely used in the industry because, even if they do not have full mobility but only four degrees of freedom, they are capable of performing Schoenflies motions, characterized by three translations and one rotation about the vertical direction. This type of mobility is sufficient for a wide variety of manipulation tasks, such as palletization, handling and assembly of objects placed on horizontal surfaces, effectively replacing more expensive anthropomorphic 6-DOF arms. Therefore, the development of SCARA-like robotic architectures with high energy efficiency is a relevant research topic, with a potentially significant impact on the sustainability of robotized lines. Other researchers have proposed leveraging the natural motion of SCARA robots for periodic motions [23,24]. In these works, the elastic elements were added to the first two revolute joints with vertical axes, giving rise to cyclic oscillations in the horizontal plane. The limitation of this approach is that the horizontal robot motions must be planned around the equilibrium position of the robot, where the elastic elements are undeformed, to exploit natural motion effectively. This condition limits the flexibility in using the robot workspace, unless additional actuators are introduced to vary the neutral position of the elastic elements based on the specific task, with the drawback of increased mechanical and control complexity.

Conversely, in the present work, natural motion is exploited for the vertical motion. This choice is motivated by the fact that SCARA robots are often used in pick-and-place or manipulation tasks in which the parts are moved across different positions located approximately on the same horizontal working plane, and that the elementary departure-and-approach motions can have the same vertical range. In these applications, the exploitation of the natural vertical motion does not constrain the horizontal trajectory, provided that the elementary displacements are performed with equal or similar periods.

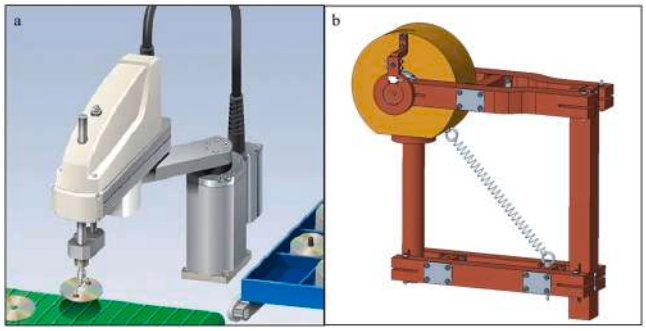

Fig. 1. SCARA robot performing a pick-and place task (a); vertical four-bar mechanism with a direct-drive actuator and elastic balancing achieved through a linear coil spring.

The remainder of the paper is organized as follows: Section 2 discusses the position and velocity kinematics of the RR-4R-R robot. Section 3 analyses the workspace of the RR-4R-R robot and compares it to that of the SCARA architecture. Section 4 outlines the dynamic model of the RR-4R-R robot, considering two possible types of natural elastic balancing: one using a torsional spring placed on a revolute joint of the four-bar mechanism, and one using a linear coil spring connecting two links of the four-bar mechanism. Section 5 discusses the natural motion of the parallelogram four-bar linkage with elastic balancing in a vertical plane, which involves the third actuator without moving the remaining actuators. Section 6 compares natural elastic balancing with exact balancing, which has the advantage of providing an indifferent equilibrium in any robot position but does not generate natural motion. Section 7 investigates the coupled dynamic effects of the whole robot motion on the vertical natural motion, assessing the validity of a simplified uncoupled model of the vertical motion. Section 8 discusses the influence of finite stop phases on the efficacy of natural and exact elastic balancing. In Section 9, the thresholds of convenience between natural and exact elastic balancing are studied for different operating conditions, also outside the resonance condition. Section 10 discusses possible tuning strategies for the case of payload variations. The last section presents the conclusions.

2. Kinematic model of the RR-4R-R robot

The kinematic scheme of the RR-4R-R robot is shown in Fig. 2. The internal coordinates are the joint angles of the actuators J1…J4, collected in the vector $\boldsymbol{\theta} = [\theta_1, \theta_2, \theta_3, \theta_4]^T$. The external coordinates are the three cartesian coordinates of the end-effector point E, and the end-effector rotation around the vertical axis, collected in the vector $\boldsymbol{x} = [x, y, z, \theta]^T$. The direct and inverse position analyses are extensively discussed in [21]. The direct position analysis can be expressed by the following equations:

$$\begin{aligned} x &= l_1 c_1 + l_3 c_3 c_{12} \\ y &= l_1 s_1 + l_3 c_3 s_{12} \\ z &= l_0 - l_3 s_3 - l_5 \\ \theta &= \theta_1 + \theta_2 + \theta_4 \end{aligned} \tag{1}$$

In Eq. (1) and in the following, for brevity, $c_i = \cos(\theta_i)$, $s_i = \sin(\theta_i)$, $c_{ij} = \cos(\theta_i+\theta_j)$, and $s_{ij} = \sin(\theta_i+\theta_j)$.

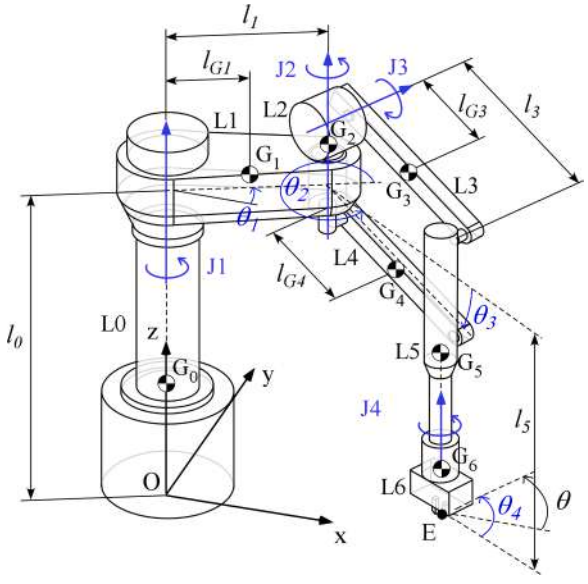

Fig. 2. Kinematic scheme of the RR-4R-R robot.

Inside the robot workspace, the inverse position analysis has two solutions for each workspace point, with opposite values of θ_2 [21]; correspondingly, there are two solutions for θ_1 and two solutions for θ_4. The inverse position analysis can be expressed by the following equations:

$$\begin{aligned} \theta_3 &= \arcsin\left(\frac{l_0 - l_5 - z}{l_3}\right) \\ \theta_2 &= \pm\text{atan2}(s_2, c_2), \text{with } c_2 = \frac{x^2 + y^2 - l_1^2 - l_3^2 c_3^2}{2 l_1 l_3 c_3} \text{ and } s_2 = \sqrt{1 - c_2^2} \\ \theta_1 &= \text{atan2}(y, x) - \text{atan2}(l_3 c_3 s_2, l_1 + l_3 c_3 c_2) \\ \theta_4 &= \theta - \theta_1 - \theta_2 \end{aligned} \tag{2}$$

The velocity analysis can be performed by differentiating the direct position equations (1), thus obtaining the Jacobian matrix **J**:

$$\dot{\mathbf{x}} = \mathbf{J}\dot{\boldsymbol{\theta}} = \begin{bmatrix} -l_1 s_1 - l_3 c_3 s_{12} & -l_3 c_3 s_{12} & -l_3 s_3 c_{12} & 0 \\ l_1 c_1 + l_3 c_3 c_{12} & l_3 c_3 c_{12} & -l_3 s_3 s_{12} & 0 \\ 0 & 0 & -l_3 c_3 & 0 \\ 1 & 1 & 0 & 1 \end{bmatrix} \dot{\boldsymbol{\theta}} \tag{3}$$

3. Comparison of the RR-4R-R and SCARA architectures

The workspace of the RR-4R-R manipulator differs from that of the SCARA robot due to the type of the third joint, which is revolute instead of prismatic. Regarding the SCARA robot, keeping the actuators 1, 2, and 4 fixed and moving only the third prismatic actuator, the end-effector performs a vertical rectilinear motion. On the contrary, keeping fixed the actuators 1, 2, and 4 of the RR-4R-R manipulator and moving only its third revolute actuator, its end-effector performs a motion which is translational but not rectilinear, with all the end-effector points following circular trajectories with radius l_3.

The workspaces of the SCARA and RR-4R-R robots are compared in Fig. 3, where the common links are represented in black, the SCARA links are represented in blue, and the RR-4R-R links are represented in green. The comparison of Fig. 3 is based on the following assumptions: equal lengths of the common links, L0 and L1; length of the SCARA forearm (link L2) equal to those of the RR-4R-R links L3 and L4; angular ranges of ±110° and ±145° for the revolute joints J1 and J2 of both robots; angular range of ±35° for the joint J3 of the RR-4R-R robot, and vertical range of the SCARA prismatic joint which provides a vertical mobility of the end-effector equal to that of the RR-4R-R robot.

In Fig. 3, the common workspace boundaries are represented in black dashed lines, the SCARA workspace boundaries are represented in blue dashed lines, and the RR-4R-R workspace boundaries are represented in green. With the considered assumptions, the two workspaces are quite similar, but the one of the RR-4R-R robot is slightly smaller than that of the SCARA. However, this lack can be compensated for by increasing the lengths of the links L3 and L4 of the RR-4R-R robot.

Observing the SCARA geometry, it is evident that to perform a pure vertical translation (variation of z with constant x, y, and θ) it is sufficient to move only the third prismatic actuator while keeping fixed the remaining ones. On the contrary, the inverse position analysis of the RR-4R-R robot, system (2), evidences that to perform a pure vertical translation it is necessary to move simultaneously all the four actuators: as a matter of fact, z influences θ_3 according to the first equation of the system (2), and then θ_3 influences θ_1, θ_2, and θ_4 according to the remaining three equations of the system (2).

On the other hand, for movements in horizontal planes (variations of x, y, and θ with constant z), the third actuator is motionless for both robots: for the SCARA robot, it is evident that the z coordinate depends only on the position of the prismatic joint; similarly, the third equation of the direct position analysis of the RR-4R-R manipulator, system (1), shows that z depends only on the internal coordinate θ_3.

4. Dynamic model of the RR-4R-R robot

The proposed robotic architecture features seven revolute joints, three of which are passive and four actuated by direct-drive motors, without interposition of mechanical transmissions. Consequently, the joints can be assumed to be frictionless, and the torque τ_i of the i th actuator can be calculated using the Lagrangian equations:

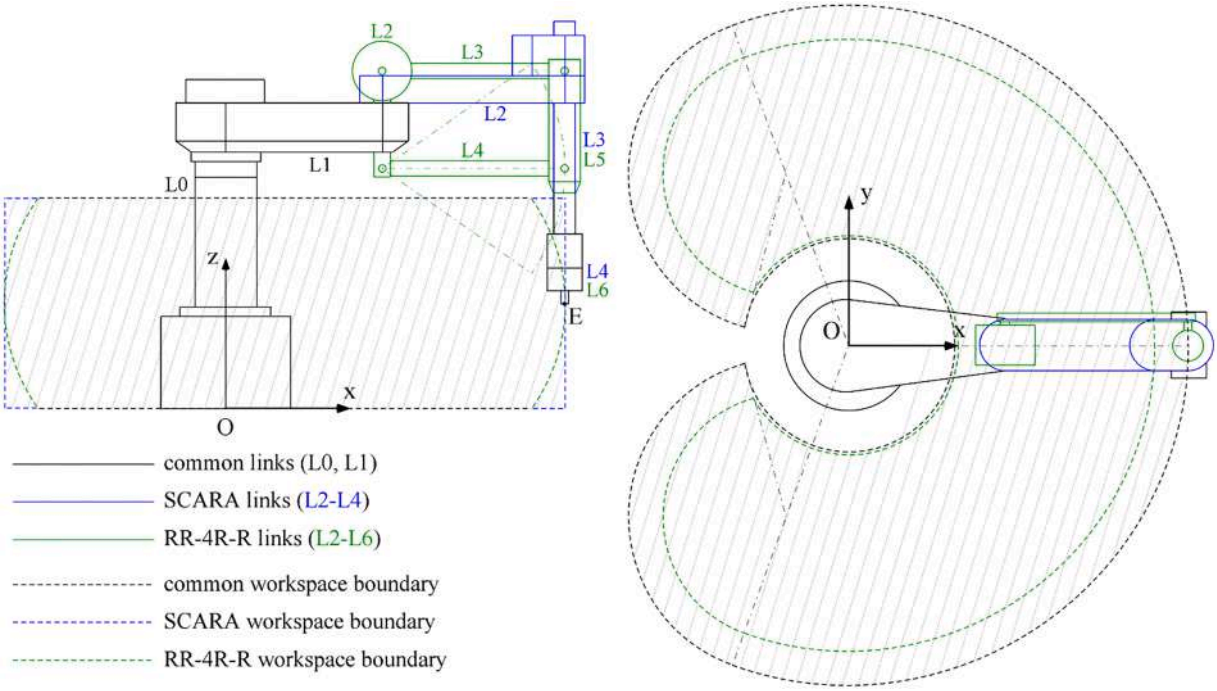

Fig. 3. Comparison of the workspaces of the SCARA and RR-4R-R robots.

$$\tau_i = \frac{d}{dt}\frac{\partial L}{\partial \dot{\theta}_i} - \frac{\partial L}{\partial \theta_i} + \sum_{j=1}^{4} J_{ji} F_j, i = 1...4 \tag{4}$$

where $L = T - V$ is the Lagrangian function, the difference between the kinetic energy T and the potential energy V, J_{ji} is the (j,i) element of the Jacobian matrix, and F_j is the j^{th} element of the vector of the generalized forces applied to the end-effector along the directions of the external coordinates, $\boldsymbol{F} = [F_x, F_y, F_z, M_z]^T$. Let us note that the M_x and M_y components of the moment are balanced by the joint reactions without influencing the actuator torques. When there is no contact between the end-effector and the environment, for example in pick-and-place tasks, the last term on the right side of (4) is zero.

The kinetic energy T of the system is the sum of the kinetic energies of the six links, $T_1 \ldots T_6$:

$$T_1 = \frac{1}{2} I_{G1} \dot{\theta}_1^2 + \frac{1}{2} m_1 l_{G1}^2 \dot{\theta}_1^2 = \frac{1}{2} I_1 \dot{\theta}_1^2 \tag{5}$$

$$T_2 = \frac{1}{2} m_2 l_1^2 \dot{\theta}_1^2 + \frac{1}{2} I_{G2} (\dot{\theta}_1 + \dot{\theta}_2)^2 \tag{6}$$

$$T_3 = \frac{1}{2} m_3 v_{G3}^2 + \frac{1}{2} \boldsymbol{\omega}_{P3}^T \mathbf{I}_{P3} \boldsymbol{\omega}_{P3} \tag{7}$$

$$T_4 = \frac{1}{2} m_4 v_{G4}^2 + \frac{1}{2} \boldsymbol{\omega}_{P4}^T \mathbf{I}_{P4} \boldsymbol{\omega}_{P4} \tag{8}$$

$$T_5 = \frac{1}{2} m_5 v_{G5}^2 + \frac{1}{2} I_{G5} (\dot{\theta}_1 + \dot{\theta}_2)^2 \tag{9}$$

$$T_6 = \frac{1}{2} m_6 v_{G6}^2 + \frac{1}{2} I_{G6} (\dot{\theta}_1 + \dot{\theta}_2 + \dot{\theta}_4)^2 \tag{10}$$

In Eqs. (5)-(10): v_{Gi} is the magnitude of the velocity of center of mass (COM) of the i th link; the three scalars m_i, I_{Gi} and I_i are respectively the mass of the i^{th} link, its moment of inertia around a vertical axis passing through its COM, and its moment of inertia around a vertical axis passing through the i^{th} joint; $\mathbf{I}_{P3}$ and $\mathbf{I}_{P4}$ are the principal inertia tensors of links L3 and L4, related to a reference frame with its origin in the COM, the x-axis along the longitudinal link direction, and the z-axis lying in a vertical plane and pointing upwards; $\boldsymbol{\omega}_{P3}$ and $\boldsymbol{\omega}_{P4}$ are the vectors of the angular velocities of the links L3 and L4, which are the only links that can rotate around a non-vertical direction; these angular velocity vectors are expressed in the same principal reference frames as $\mathbf{I}_{P3}$ and $\mathbf{I}_{P4}$.

The velocity vectors of the COM of L5 and L6, $\mathbf{v}_{G5}$ and $\mathbf{v}_{G6}$, are equal and can be obtained from the first three rows of the Jacobian matrix (3):

$$\mathbf{v}_{G5} = \mathbf{v}_{G6} = \begin{bmatrix} \dot{x} \\ \dot{y} \\ \dot{z} \end{bmatrix} = \begin{bmatrix} -l_1 s_1 \dot{\theta}_1 - l_3 s_3 c_{12} \dot{\theta}_3 - l_3 c_3 s_{12} (\dot{\theta}_1 + \dot{\theta}_2) \\ l_1 c_1 \dot{\theta}_1 - l_3 s_3 s_{12} \dot{\theta}_3 + l_3 c_3 c_{12} (\dot{\theta}_1 + \dot{\theta}_2) \\ -l_3 c_3 \dot{\theta}_3 \end{bmatrix} \tag{11}$$

It is easy to demonstrate that the velocity vectors of the COM of L3 and L4, $\mathbf{v}_{G3}$ and $\mathbf{v}_{G4}$, can be expressed by Eq. (11), but replacing l_3 with l_{G3} for $\mathbf{v}_{G3}$, and replacing l_3 with l_{G4} for $\mathbf{v}_{G4}$.

The angular velocities $\boldsymbol{\omega}_{P3}$ and $\boldsymbol{\omega}_{P4}$ are equal due to the parallelogram shape of the four-bar. They are the sum of an angular velocity vector with magnitude $\dot{\theta}_3$ along the joint axis J3, and an angular velocity vector with magnitude $(\dot{\theta}_1 + \dot{\theta}_2)$ along the joint axis J2. The axis J3 corresponds to the y-axis of the principal reference frame used for $\mathbf{I}_{P3}$ and $\mathbf{I}_{P4}$, while the axis J2 lies in the xz plane of the same reference, with inclination θ_3 with respect to its z-axis. Considering these orientations, the vectors $\boldsymbol{\omega}_{P3}$ and $\boldsymbol{\omega}_{P4}$ can be expressed as follows:

$$\boldsymbol{\omega}_{P3} = \boldsymbol{\omega}_{P4} = \begin{bmatrix} -s_3 (\dot{\theta}_1 + \dot{\theta}_2) \\ \dot{\theta}_3 \\ c_3 (\dot{\theta}_1 + \dot{\theta}_2) \end{bmatrix} \tag{12}$$

Considering Eqs. (11) and (12), and the fact that the principal inertia tensors $\mathbf{I}_{P3}$ and $\mathbf{I}_{P4}$ are diagonal with diagonal values I_{Pjxx}, I_{Pjyy}, and I_{Pjzz}, where $j = 3,4$, the overall kinetic energy can be expressed as follows:

$$T = \sum_{i=1}^{6} T_i = \frac{1}{2} \left(k_{T1} \dot{\theta}_1^2 + k_{T2} (\dot{\theta}_1 + \dot{\theta}_2)^2 + k_{T3} (\dot{\theta}_1 + \dot{\theta}_2 + \dot{\theta}_4)^2 + k_{T4} \dot{\theta}_3^2 + \right.$$
$$\left. + k_{T5} c_3^2 (\dot{\theta}_1 + \dot{\theta}_2)^2 + k_{T6} s_3^2 (\dot{\theta}_1 + \dot{\theta}_2)^2 - k_{T7} s_2 s_3 \dot{\theta}_1 \dot{\theta}_3 + k_{T7} c_2 c_3 \dot{\theta}_1 (\dot{\theta}_1 + \dot{\theta}_2) \right) \tag{13}$$

where the six constants $k_{T1} \ldots k_{T6}$ are defined by the following expressions:

$$k_{T1} = I_1 + (m_2 + m_3 + m_4 + m_5 + m_6) l_1^2 \tag{14}$$

$$k_{T2} = I_{G2} + I_{G5} \tag{15}$$

$$k_{T3} = I_{G6} \tag{16}$$

$$k_{T4} = m_3 l_{G3}^2 + m_4 l_{G4}^2 + (m_5 + m_6) l_3^2 + I_{P3yy} + I_{P4yy} \tag{17}$$

$$k_{T5} = m_3 l_{G3}^2 + m_4 l_{G4}^2 + (m_5 + m_6) l_3^2 + I_{P3zz} + I_{P4zz} \tag{18}$$

$$k_{T6} = I_{P3xx} + I_{P4xx} \tag{19}$$

$$k_{T7} = 2 l_1 (m_3 l_{G3} + m_4 l_{G4} + (m_5 + m_6) l_3) \tag{20}$$

The potential energy V is the sum of the gravitational energy V_g and the elastic energy V_e. The gravitational energy of the system is obtained by summing the gravitational energies of the links L3, L4, L5, and L6, since those of the links L1 and L2 are constant:

$$V_g = -m_3 g l_{G3} s_3 - m_4 g l_{G4} s_3 - m_5 g l_3 s_3 - m_6 g l_3 s_3 + V_{g0} =$$
$$= -m_{eq} g l_3 s_3 + V_{g0}, \text{with} m_{eq} = m_5 + m_6 + m_3 \frac{l_{G3}}{l_3} + m_4 \frac{l_{G4}}{l_3} \tag{21}$$

where V_{g0} is an arbitrary constant.

The elastic energy V_e is zero in the absence of elastic balancing; in the presence of elastic balancing, its formulation depends on the configuration of the elastic elements. Two types of elastic balancing are hereby considered:

- *elastic balancing with torsional spring* (TS): a torsional spring with stiffness k_{ts} is placed on one of the revolute joints of the vertical four-bar; it is possible to use more torsional springs placed on different revolute joints, and this doesn't change the dynamic model, as long as the stiffnesses of the various springs are added together to obtain an overall equivalent stiffness k_{ts};
- *elastic balancing with linear coil spring* (LS): a linear spring with stiffness k_{ls} and undeformed length l_{und} connects point S_2 of link L2 and point S_4 of link L4 (Fig. 4).

4.1. Elastic balancing with torsional spring

The elastic potential energy in the case of elastic balancing with torsional spring is:

$$V_{e,ts} = \frac{1}{2} k_{ts} (\theta_3 - \theta_{3n})^2 \tag{22}$$

where θ_{3n} is the preload angle at which the spring is undeformed. Therefore, the Lagrangian function L of the system in the case of elastic balancing with torsional spring is:

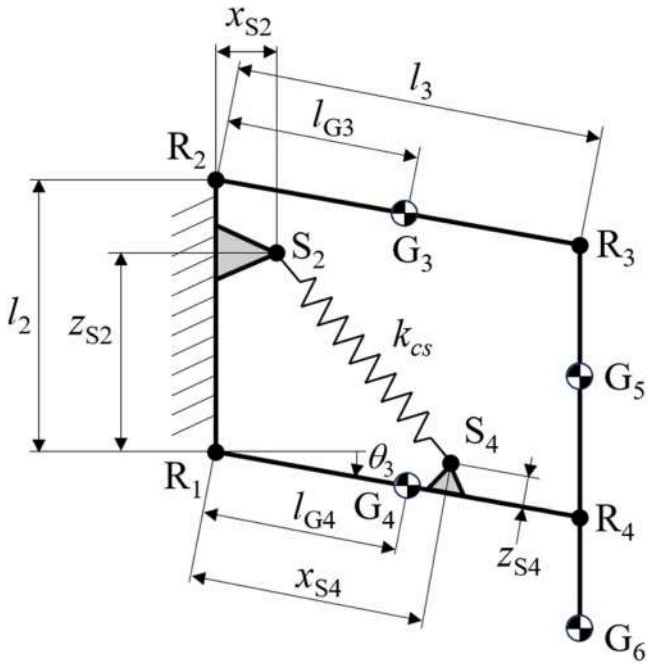

Fig. 4. Scheme of the parallelogram four-bar linkage with elastic balancing by linear coil spring (LS).

$$L_{ts} = T - V_g - V_{e,ts} = \\ = \frac{1}{2}\left(k_{T1}\dot{\theta}_1^2 + k_{T2}(\dot{\theta}_1+\dot{\theta}_2)^2 + k_{T3}(\dot{\theta}_1+\dot{\theta}_2+\dot{\theta}_4)^2 + k_{T4}\dot{\theta}_3^2 \right. \\ \left. + k_{T5}c_3^2(\dot{\theta}_1+\dot{\theta}_2)^2 + k_{T6}s_3^2(\dot{\theta}_1+\dot{\theta}_2)^2 + -k_{T7}s_2s_3\dot{\theta}_1\dot{\theta}_3 + k_{T7}c_2c_3\dot{\theta}_1(\dot{\theta}_1+\dot{\theta}_2)\right) \\ + m_{eq}gl_3s_3 - V_{g0} - \frac{1}{2}k_{ts}(\theta_3-\theta_{3n})^2 \tag{23}$$

The actuator torques τ_i can be obtained through Eq. (4), starting from the Lagrangian function (23). In particular, it is useful to evaluate the expression of the torque of the third actuator with the assumption of no external force acting on the end-effector, since the objective of the work is to reduce this torque in free-motion tasks by exploiting the robot's natural motion:

$$\tau_3 = I_{eq}\ddot{\theta}_3 - m_{eq}gl_3c_3 + k_{ts}(\theta_3-\theta_{3n}) - \frac{k_{T7}}{2}s_2s_3\ddot{\theta}_1 + \frac{k_{T7}}{2}c_2s_3\dot{\theta}_1^2 \\ + (k_{T5}-k_{T6})s_3c_3(\dot{\theta}_1+\dot{\theta}_2)^2 \tag{24}$$

In Eq. (24), the constant $I_{eq} = k_{T4}$ corresponds to the equivalent inertia of the four-bar moving in a vertical plane with the actuators J1 and J2 motionless. As a matter of fact, the last three terms of the right side of Eq. (24) represent the effects on the third actuator of the inertial forces caused by the motion of J1 and J2. These inertial effects are zero when θ_1 and θ_2 are constant.

4.2. Elastic balancing with linear coil spring

The elastic potential energy in the case of elastic balancing with a linear coil spring is:

$$V_{e,ls} = \frac{1}{2}k_{ls}(\overline{S_2S_4}(\theta_3) - l_{und})^2 \tag{25}$$

The distance between the S_2 and S_4 can be obtained by analysing the geometry represented in Fig. 4; its expression is:

$$\overline{S_2S_4}(\theta_3) = \sqrt{(x_{S2} - x_{S4}c_3 - z_{S4}s_3)^2 + (z_{S2} + x_{S4}s_3 - z_{S4}c_3)^2} \\ = \sqrt{A + Bc_3 + Cs_3} \text{with}: A = x_{S2}^2 + z_{S2}^2 + x_{S4}^2 + z_{S4}^2 B \\ = -2(x_{S2}x_{S4} + z_{S2}z_{S4})C = 2(z_{S2}x_{S4} - x_{S2}z_{S4}) \tag{26}$$

where the length parameters x_{S2}, z_{S2}, x_{S4}, and z_{S4} represent the positions of the two spring attachment points (Fig. 4). When the links L3 and L4 are horizontal ($\theta_3 = 0$), Eq. (25) expresses the length of the spring in this position, $l_o = (A + B)^{1/2}$. The Lagrangian function of the system in the case of elastic balancing with a linear coil spring is:

$$L_{ls} = T - V_g - V_{e,ls} = \\ = \frac{1}{2}\left(k_{T1}\dot{\theta}_1^2 + k_{T2}(\dot{\theta}_1+\dot{\theta}_2)^2 + k_{T3}(\dot{\theta}_1+\dot{\theta}_2+\dot{\theta}_4)^2 + k_{T4}\dot{\theta}_3^2 \right. \\ \left. + k_{T5}c_3^2(\dot{\theta}_1+\dot{\theta}_2)^2 + k_{T6}s_3^2(\dot{\theta}_1+\dot{\theta}_2)^2 + -k_{T7}s_2s_3\dot{\theta}_1\dot{\theta}_3 + k_{T7}c_2c_3\dot{\theta}_1(\dot{\theta}_1+\dot{\theta}_2)\right) \\ + m_{eq}gl_3s_3 - V_{g0} - \frac{1}{2}k_{ls}\left(\sqrt{A + Bc_3 + Cs_3} - l_{und}\right)^2 \tag{27}$$

Starting from the Lagrangian function (27), the torque τ_3 with the assumption of no external force acting on the end-effector can be obtained by the Lagrange Eq. (4):

$$\tau_3 = I_{eq}\ddot{\theta}_3 - m_{eq}gl_3c_3 + k_{ls}\frac{\sqrt{A + Bc_3 + Cs_3} - l_{und}}{2\sqrt{A + Bc_3 + Cs_3}}(Cc_3 - Bs\theta_3) - \frac{k_{T7}}{2}s_2s_3\ddot{\theta}_1 \\ + \frac{k_{T7}}{2}c_2s_3\dot{\theta}_1^2 + (k_{T5}-k_{T6})s_3c_3(\dot{\theta}_1+\dot{\theta}_2)^2 \tag{28}$$

As in Eq. (24), the last three terms of the right side of Eq. (28) represent the inertial effects on J3 of the motion of J1 and J2, which are zero when θ_1 and θ_2 are constant.

The type of elastic balancing influences the elastic energy and V_e, but not the kinetic energy T nor the gravitational energy V_g; moreover, in all cases the elastic energy is function only of θ_3. Consequently, the expressions of the motor torques τ_1, τ_2, and τ_4, which can be obtained by Eq. (4), are independent of the type of balancing:

$$\tau_1 = (k_{T1}+k_{T2}+k_{T3})\ddot{\theta}_1 + (k_{T2}+k_{T3})\ddot{\theta}_2 + k_{T3}\ddot{\theta}_4 + \left(k_{T5}c_3^2 \right. \\ \left. + k_{T6}s_3^2\right)\left(\ddot{\theta}_1+\ddot{\theta}_2\right) + 2(k_{T6}-k_{T5})s_3c_3\dot{\theta}_3(\dot{\theta}_1+\dot{\theta}_2) + +\frac{1}{2}k_{T7}\left(c_2c_3\left(2\ddot{\theta}_1 \right.\right. \\ \left.\left. + \ddot{\theta}_2\right) - (s_2c_3\dot{\theta}_2 + c_2s_3\dot{\theta}_3)(2\dot{\theta}_1+\dot{\theta}_2) - (c_2s_3\dot{\theta}_2 + s_2c_3\dot{\theta}_3)\dot{\theta}_3 - s_2s_3\ddot{\theta}_3\right) \tag{29}$$

$$\tau_2 = (k_{T2}+k_{T3})\ddot{\theta}_1 + (k_{T2}+k_{T3})\ddot{\theta}_2 + k_{T3}\ddot{\theta}_4 + \left(k_{T5}c_3^2 + k_{T6}s_3^2\right)\left(\ddot{\theta}_1+\ddot{\theta}_2\right) \\ + 2(k_{T6}-k_{T5})s_3c_3\dot{\theta}_3(\dot{\theta}_1+\dot{\theta}_2) + \quad + \frac{1}{2}k_{T7}\left(c_2c_3\ddot{\theta}_1 + s_2c_3\dot{\theta}_1^2\right) \tag{30}$$

$$\tau_4 = k_{T3}\left(\ddot{\theta}_1+\ddot{\theta}_2+\ddot{\theta}_4\right) \tag{31}$$

The expressions of the motor torques, Eqs. (24), (28), (29), (30), and (31), show that the dynamics of the RR-4R-R robot is highly coupled. Unlike the SCARA robot, the torque of the third actuator J3, which drives the vertical motion, is influenced by the inertial effects related to the horizontal motions driven by the joints J1 and J2, as represented by

the last three terms of Eqs. (24) and (28). This effect must be considered in the sizing of the actuator J3. Moreover, the replacement of the vertical prismatic joint, usually realized in SCARA robots by means of a compact ball-screw mechanism, with a four-bar mechanism actuated by a direct-drive motor and equipped with an elastic element can probably increase the overall robot mass, thus limiting the achievable accelerations of the joints J1 and J2. Nevertheless, the negative effect of the increase in the moving masses is compensated by the fact that the four-bar actuator J3 is vertically aligned with the end of link L1, and not with the end-effector. Consequently, when the robot arm is extended and the effector is close to the external workspace boundary (θ_2 close to zero), which is the worst dynamic condition for the actuator J1, the moment of inertia of the four-bar actuator reflected to joint J1 is probably lower than that of the prismatic actuation system of the SCARA. Conversely, when the end-effector is close to the internal workspace boundary (θ_2 close to its upper or lower limit), it is favourable for the inertia reflected to J1 to have the third actuator vertically aligned with the end-effector. However, the placement of the third actuator at a fixed distance from the axis of joint J1, as in the RR-4R-R robot, reduces the variations of the overall inertia reflected to this axis, which is in general favourable for the control tuning. As regards the inertia reflected to J2, the placement of the third actuator in the RR-4R-R manipulator, aligned with joint J2, is favourable compared to that of the SCARA robot. In general, the exact comparison of the dynamic performances of the two robots depends on the detailed embodiment design and on the required trajectory.

5. Natural motion of the parallelogram four-bar linkage with elastic balancing in a vertical plane

In this section, we consider in the first instance the motion of the four-bar linkage in a vertical plane, with θ_1 and θ_2 constant, to obtain a simplified expression of the natural motion. The assumption of constant θ_1 and θ_2 does not influence the expressions of the potential energies V_g and V_e, Eqs. (21), (22) and (25), since they are functions only of the internal coordinate θ_3. On the contrary, this hypothesis simplifies the expression of the kinetic energy.

5.1. Elastic balancing with torsional spring

With the assumption of joints J1 and J2 motionless, Eq. (23) becomes:

$$L_{ts} = \frac{1}{2} I_{eq} \dot{\theta}_3^2 + m_{eq} g l_3 s_3 - V_{g0} - \frac{1}{2} k_{ts} (\theta_3 - \theta_{3n})^2 \tag{32}$$

Consequently, Eq. (24) can be simplified as follows:

$$\tau_3 = I_{eq} \ddot{\theta}_3 - m_{eq} g l_3 c_3 + k_{ts} (\theta_3 - \theta_{3n}) = \tau_{3in} - \tau_{3g} + \tau_{3el,ts} \tag{33}$$

In Eq. (33) the three terms, τ_{3in}, τ_{3g}, and $\tau_{3el,ts}$, represent respectively the inertial, gravitational and elastic effects. Eq. (33) can be used to obtain the relationship between the negative preload angle and the torsional spring stiffness in order to obtain an exact elastic balancing in static conditions, with zero motor torque, when links L3 and L4 are horizontal ($\theta_3 = 0$); imposing zero actuation torque, angle, and acceleration in (33) we obtain:

$$\theta_{3n} = -\frac{m_{eq} g l_3}{k_{ts}} = -\left(m_5 + m_6 + m_3 \frac{l_{G3}}{l_3} + m_4 \frac{l_{G4}}{l_3} \right) \frac{g l_3}{k_{ts}} \tag{34}$$

The nonlinear differential equation of the natural motion in the case of elastic balancing with torsional spring can be obtained by imposing zero actuation torque in (33):

$$I_{eq} \ddot{\theta}_3 - m_{eq} g l_3 c_3 + k_{ts} (\theta_3 - \theta_{3n}) = 0 \tag{35}$$

5.2. Elastic balancing with linear coil spring

With the assumption of joints J1 and J2 motionless, Eq. (27) becomes:

$$\begin{aligned} L_{ls} &= T - V_g - V_e \\ &= \frac{1}{2} I_{eq} \dot{\theta}_3^2 + m_{eq} g l_3 s_3 - V_{g0} - \frac{1}{2} k_{ls} \left(\sqrt{A + B c_3 + C s_3} - l_{und} \right)^2 \end{aligned} \tag{36}$$

Consequently, Eq. (28) can be simplified as follows:

$$\begin{aligned} \tau_3 &= I_{eq} \ddot{\theta}_3 - m_{eq} g l_3 c_3 + k_{ls} \frac{\sqrt{A + B c_3 + C s_3} - l_{und}}{2\sqrt{A + B c_3 + C s_3}} (C c_3 - B s_3) \\ &= \tau_{3in} - \tau_{3g} + \tau_{3el,ls} \end{aligned} \tag{37}$$

In Eq. (37) the first two terms, inertial and gravitational, are equal to those of Eq. (33), while the elastic term $\tau_{3el,ls}$ is nonlinear, unlike Eq. (33). Eq. (37) can be used to obtain the relationship among the spring parameters (l_{und} and k_{ls}) and the placement of the attachment points S_2 and S_4 (which determine the constants A, B and C) which is necessary to impose exact balancing in static conditions, with zero motor torque, when links L3 and L4 are horizontal ($\theta_3 = 0$); imposing zero actuation torque, angle and acceleration in (37), we obtain:

$$l_o - l_{und} = \sqrt{A + B} - l_{und} = \frac{2 m_{eq} g l_o l_3}{C k_{ls}} = \frac{m_{eq} g l_o l_3}{k_{ls} (z_{P2} x_{P4} - x_{P2} z_{P4})} \tag{38}$$

Eq. (38) can be used in different ways, for example for determining l_{und} and k_{ls} once the attachment points are defined. It is important to note that the spring parameters and the placement of the attachment points determine the natural period of the vertical motion, as it will be discussed in the following.

The nonlinear differential equation of the natural motion in the case of elastic balancing with linear coil spring can be obtained by imposing zero actuation torque in (37):

$$I_{eq} \ddot{\theta}_3 - m_{eq} g l_3 c_3 + k_{ls} \frac{\sqrt{A + B c_3 + C s_3} - l_{und}}{2\sqrt{A + B c_3 + C s_3}} (C c_3 - B s_3) = 0 \tag{39}$$

5.3. Comparison of natural motion with torsional spring and with linear coil spring

The nonlinear dynamic model of the system's natural motion in the case of elastic balancing with torsional spring, represented by (35), can be linearized by a first-order Taylor polynomial expansion, obtaining:

$$I_{eq} \ddot{\theta}_3 + k_{ts} \theta_3 = m_{eq} g l_3 + k_{ts} \theta_{3n} \tag{40}$$

When condition (34) is imposed, the constant term on the right side of Eq. (40) is zero, and the natural oscillations are centred around $\theta_3 = 0$; the linearized system is an undamped oscillator with natural period T_n:

$$T_n = \frac{2\pi}{\omega_n} = \frac{2\pi}{\sqrt{k_{ts} / I_{eq}}} \tag{41}$$

Similarly, the nonlinear dynamic model of the system's natural motion in the case of elastic balancing with linear coil spring, represented by (39), can be linearized by a first-order Taylor polynomial expansion as follows:

$$\begin{aligned} &I_{eq} \ddot{\theta}_3 + \frac{k_{ls}}{2} \left(\frac{B \left(l_{und} - \sqrt{A + B} \right) + \frac{C^2}{2\sqrt{A+B}}}{\sqrt{A + B}} + \frac{C^2 \left(l_{und} - \sqrt{A + B} \right)}{2 (A + B)^{\frac{3}{2}}} \right) \theta_3 \\ &= m_{eq} g l_3 + \frac{k_{ls} C \left(l_{und} - \sqrt{A + B} \right)}{2\sqrt{A + B}} \end{aligned} \tag{42}$$

After some algebraic manipulation, the linear differential Eq. (42) can be rewritten in a more compact form:

$$I_{eq} \ddot{\theta}_3 + \frac{k_{ls}}{2} \left(\frac{C^2 l_{und}}{2 l_o^3} - B \frac{l_o - l_{und}}{l_o} \right) \theta_3 = m_{eq} g l_3 - \frac{k_{ls} C (l_o - l_{und})}{2 l_o} \tag{43}$$

When the condition (38) is imposed, the constant term on the right

side of Eq. (43) is zero, and the natural oscillations are centred around $\theta_3 = 0$; the linearized system is an undamped oscillator with natural period T_n:

$$T_n = \frac{2\pi}{\omega_n} = \frac{2\pi}{\sqrt{\frac{k_{ls}}{2I_{eq}}\left(\frac{C^2 l_{und}}{2l_o^3} - B\frac{l_o - l_{und}}{l_o}\right)}} \tag{44}$$

By comparing Eqs. (40) and (43), it is possible to observe that for small oscillations a linear coil spring with stiffness k_{ls} corresponds to a torsional spring with the following equivalent stiffness:

$$k_{ts,eq} = \frac{k_{ls}}{2}\left(\frac{C^2 l_{und}}{2l_o^3} - B\frac{l_o - l_{und}}{l_o}\right) \tag{45}$$

Condition (45) involves both the linear coil spring parameters, l_{und} and k_{ls}. If the torsional stiffness $k_{ts,eq}$ is given, the linear coil spring parameters can be obtained using Eqs. (38) and (45), yielding the following expressions:

$$k_{ls} = \frac{4l_o^2}{C^2}\left(k_{ts,eq} + \frac{m_{eq} g l_3}{C}\left(B + \frac{C^2}{2l_o^2}\right)\right) \tag{46}$$

$$l_{und} = l_o - \frac{2m_{eq} g l_3}{\frac{4l_o}{C}\left(k_{ts,eq} + \frac{m_{eq} g l_3}{C}\left(B + \frac{C^2}{2l_o^2}\right)\right)} \tag{47}$$

It is useful to compare the nonlinear models (35) and (39) with the corresponding linearized models (40) and (43). The last two linear models are equivalent when conditions (34) and (38) are fulfilled and $k_{ts} = k_{ts,eq}$, according to Eq. (45). In the following, it is assumed that these conditions are satisfied, therefore, a single linear model is considered. For example, Fig. 5 shows a comparison of the free vibration responses of the nonlinear model with torsional spring ($\theta_{3,ts}$), the nonlinear model with linear coil spring ($\theta_{3,ls}$), and the linear model ($\theta_{3,lin}$). Three cases are shown, all with a zero initial velocity, but with different initial positions: $\theta_{3,0} = 1°$, 5°, and 20°. The robot parameters are: $l_3 = 500$ mm, $l_{G3} = l_{G4} = 250$ mm, $m_3 = m_4 = 2$ kg, $m_5 = 4$ kg, $m_6 = 2$ kg, $I_{P3yy} = I_{P4yy} = 0.0417$ kgm^2. For the linear coil spring, the attachment points are defined by the parameters $x_{S2} = 66.7$ mm, $z_{S2} = 360$ mm, $x_{S4} = 350$ mm, and $z_{S4} = 50$ mm. The linear coil spring stiffness has been selected imposing a ratio $l_{und}/l_o = 0.6$; with this assumption, it is possible to calculate the linear spring stiffness $k_{ls} = 799.7$ N/m by Eq. (38), the torsional spring stiffness $k_{ts} = 54.16$ Nm/rad by Eq. (45), and the preload angle $\theta_{3n} = -41.51°$ by Eq. (34). These values correspond to a natural period of the linear system $T_n = 1.1561$ s.

Table 1
Free vibration response in the vertical plane; maximum absolute values of θ_3 and natural period for the linear model (*lin*), the nonlinear model with torsional spring (*ts*), and the nonlinear model with linear coil spring (*ls*); in parentheses, the percentage differences w.r.t. the linear model.

$\theta_{3,0}$ [°]	$\lvert\min(\theta_{3,ts})\rvert$ [°]	$\lvert\min(\theta_{3,ls})\rvert$ [°]	$T_{n,ts}$ [s]	$T_{n,ls}$ [s]
1°	1.0042 (+0.33 %)	1.0038 (+0.38 %)	1.1561	1.1561
5°	5.108 (+2.16 %)	4.884 (−2.32 %)	1.1565 (+0.03 %)	1.1571 (+0.09 %)
20°	21.843 (+9.22 %)	18.249 (−8.75 %)	1.1646 (+0.74 %)	1.1710 (+1.29 %)

It is possible to note that for $\theta_{3,0} = 1°$ the responses of the three models are nearly equal, while the differences increase while increasing the amplitudes of the natural oscillations. While the linear model has positive and negative peaks equal to the initial angle, and a natural period independent of the initial condition, for the two nonlinear models the negative peaks and the natural period depend on the initial conditions. The absolute values of the negative peaks of θ_3 and the natural periods of the nonlinear models are collected in Table 1 for $\theta_{3,0} = 1°$, 5° and 20°, along with the corresponding variations with respect to the linear model.

The values collected in Table 1 show that the errors in the estimations of the natural period using the simplified linear model are very limited, <0.1 % for oscillation amplitudes of 5°, and <1.3 % for oscillation amplitudes of 20°. The results of Fig. 5 and Table 1 are referred to $m_6 = 2$ kg, obtained as the sum of a payload mass $m_p = 0.5$ kg, and of an end-effector mass $m_{ee} = 1.5$ kg. Obviously, the natural period is influenced by the payload mass. According to (41), the natural period is proportional to the square root of $I_{eq} = k_{T4}$; according to the Eq. (17), I_{eq} is the sum of different terms, one of which depends on $m_6 = m_p + m_{ee}$. Fig. 6 shows the graph of the natural period T_n as a function of m_p, ranging from 0 kg to 2 kg, calculated according to Eq. (41), with the previously considered geometrical and inertial parameters.

In the considered payload range, the natural period variations with respect to the previously considered case ($m_p = 0.5$ kg) are not negligible (−3.5÷+27.0 %). To fully exploit the natural motion for energy-saving purposes, this effect can be compensated by adjusting the vertical motion period according to the presence and magnitude of the payload.

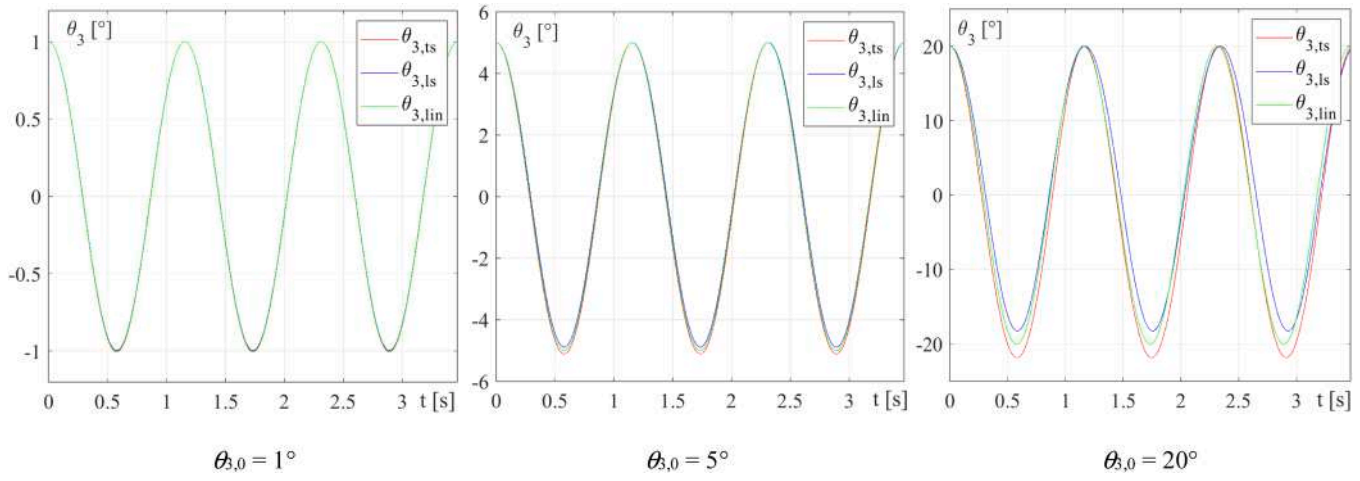

Fig. 5. Comparison of the free vibration response in the vertical plane for the nonlinear model with torsional spring ($\theta_{3,ts}$), the nonlinear model with linear coil spring ($\theta_{3,ls}$), and the linear model ($\theta_{3,lin}$), with zero initial velocity and different initial positions ($\theta_{3,0} = 1°$, 5°, and 20°).

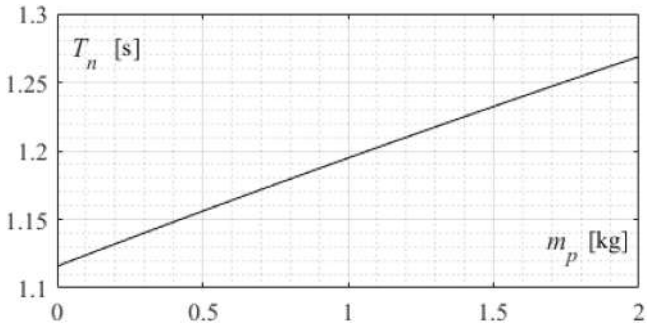

Fig. 6. Natural period T_n as a function of the payload mass m_p.

However, as discussed in Section 9, the benefits of the natural motion are not strictly limited to exact resonance (vertical motion period coinciding with the natural period), but extend to a range of operating conditions near resonance. Consequently, in the case of payload mass variation (for example, in pick-and-place operations), the exploitation of natural balancing is still favourable. The effects of payload mass variation and possible tuning approaches to face this issue are discussed in Section 10.

6. Comparison of natural and exact elastic balancing

In order to assess the profitability of natural motion, it is necessary to compare it with other types of balancing. Mass balancing (MB) can be obtained by adding proper counterweights to the links, obtaining indifferent equilibrium in any position. This type of balancing is favourable for slow motions, but the added mass increases the inertial effects and, consequently, the energy consumption for fast motions. An indifferent equilibrium in any robot position can also be obtained by means of elastic elements, for example, by designing a non-linear torsional spring based on Eq. (33) or using a zero free-length linear spring, as discussed in [25]. This type of exact gravity compensation (EB) presents the same advantages of MB for slow motions, without the drawback of a significant mass increase. Therefore, in the following comparison, MB will not be considered. While EB is favourable for slow motions, since no actuation torque is required in any static condition, no natural motion arises since the overall potential energy is constant. Consequently, natural balancing (TS or LS) can become rewarding for fast cyclic motions.

A multibody model of the RR-4R-R manipulator has been developed robot in the Simscape Multibody environment, considering the following geometrical and inertial parameters: $l_0 = 900$ mm, $l_1 = 500$ mm, $l_{G1} = 250$ mm, $l_2 = 400$ mm, $l_3 = 500$ mm, $l_{G3} = l_{G4} = 250$ mm, $l_5 =$

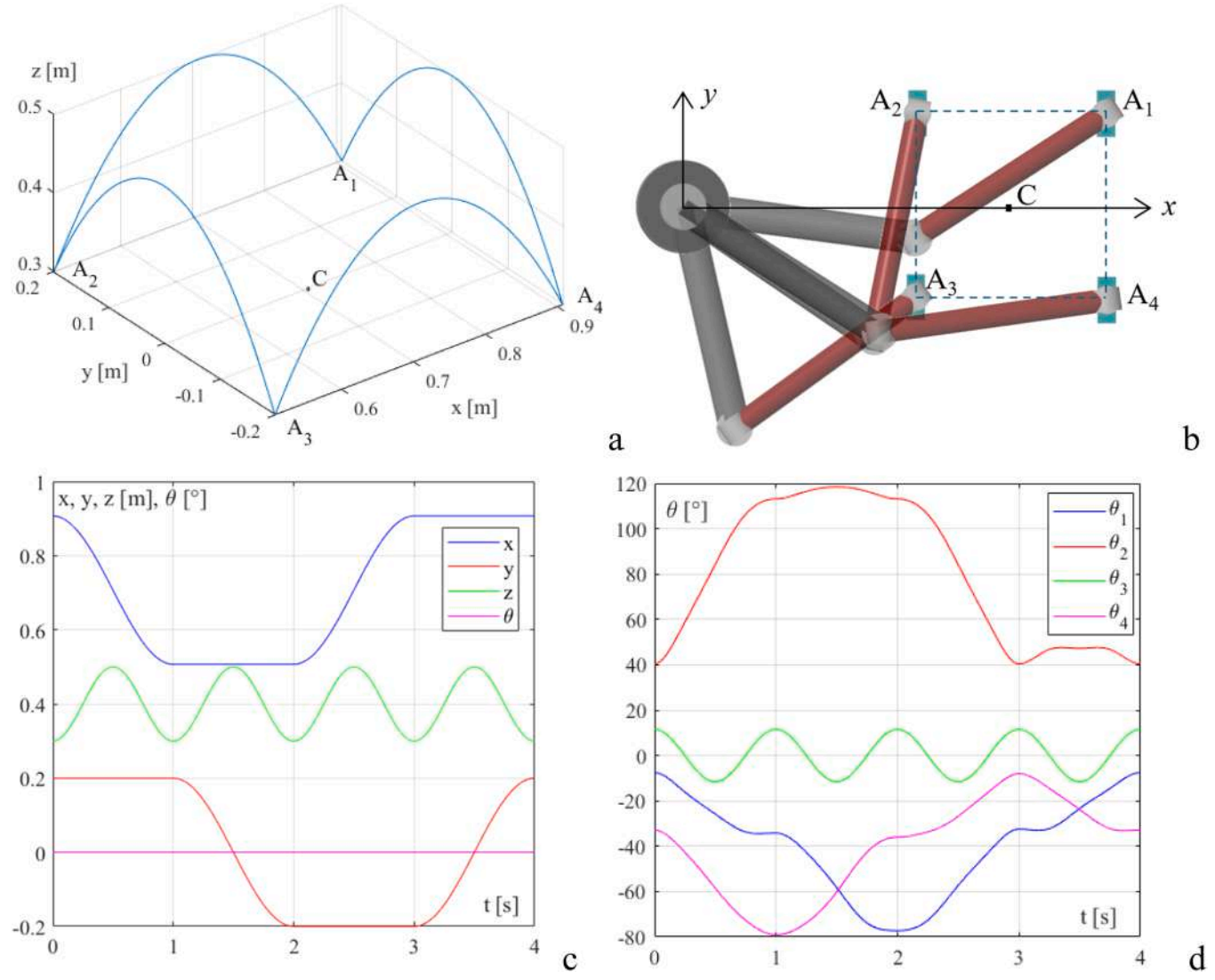

Fig. 7. Square reference trajectory S (a, b), with the corresponding external coordinates (c) and internal coordinates (d), $T_{vert} = 1$ s.

500 mm, $m_1 = 5$ kg, $I_{G1} = 1.04{\cdot}10^{-1}$ kgm^2, $m_2 = 3.5$ kg, $I_{G2} = 1.10{\cdot}10^{-3}$ kgm^2, $m_3 = m_4 = 2$ kg, $I_{P3yy} = I_{P4yy} = I_{P3zz} = I_{P4zz} = 4.17{\cdot}10^{-2}$ kgm^2, $I_{P3xx} = I_{P4xx} = 6.25{\cdot}10^{-4}$ kgm^2, $m_5 = 4$ kg, $I_{G5} = 1.30{\cdot}10^{-3}$ kgm^2, $m_6 = 2$ kg, $I_{G6} = 5.12{\cdot}10^{-5}$ kgm^2.

An example square reference trajectory S is considered, composed of four elementary movements passing through the four vertices of a square with centre in C: $A_1 = [x_C{+}d_t,\ d_t,\ z_C]$, $A_2 = [x_C{-}d_t,\ d_t,\ z_C]$, $A_3 = [x_C{-}d_t,\ -d_t,\ z_C]$, and $A_4 = [x_C{+}d_t,\ -d_t,\ z_C]$, with $d_t = 0.2$ m (Fig. 7, a). The coordinates of the square centre are $x_C = 0.707$ m, $y_C = 0$ m, $z_C = 0.300$ m, which correspond to the internal coordinates $\theta_{1C} = -45°$, $\theta_{2C} = 90°$, $\theta_{3C} = 11.537°$. In the whole reference trajectory, the external coordinate θ is set to zero, so the end-effector orientation is constant (Fig. 7, c). In the middle of each elementary movement, the end effector rises of $h_t = 0.2$ m, with the z coordinate following a sinusoidal law with amplitude $h_t/2$, period $T_{vert} = 1$ s, and mean value $l_0 - l_5 = 0.4$ m (Fig. 7, c); consequently, the end-effector oscillates symmetrically in the vertical direction around the position with links L3 and L4 horizontal ($\theta_3 = 0°$, Fig. 7, d). When $\theta_3 = 0°$ the robot is statically balanced since the elastic elements are tuned respecting conditions (34) and (38) respectively in the TS and LS cases. In the four elementary movements A_iA_{i+1}, while one of the x and y coordinates is constant, the other varies sinusoidally with period $2T_{vert}$ (Fig. 7, c). It is easy to demonstrate that this type of motion, with the horizontal period double that the vertical period, is characterized by four parabolic trajectories in vertical planes passing through the sides of the square $A_1A_2A_3A_4$ (Fig. 7, a).

Fig. 8 shows the actuator torques $\tau_1 \ldots \tau_4$ obtained by multibody simulation for the reference trajectory S, comparing the EB, TS and LS balancing approaches and the case of absence of balancing (WB). The balancing type influences only τ_3. In the comparison of Fig. 8, for the TS and LS cases, the elastic elements are tuned by means of Eqs. (41), (46), and (47) to obtain a natural period $T_n = 0.7$ s, which is lower than the vertical motion period $T_{vert} = 1$ s.

Observing Fig. 8, it is possible to note that EB correctly compensates the gravity effects which are remarkable in the WB case, shifting the time-history of τ_3 around a null mean value, and remarkably lowering the maximum absolute value of τ_3 ($\tau_{3,max}$). The torque in the EB case is due only to the inertial effects. In the TS and LS cases, the magnitude of τ_3 is similar to that of the EB case since natural motion is not fully exploited (T_n is significantly different from T_{vert}). The influence of the tuning of the elastic elements on τ_3 is shown in Fig. 9, which shows the time-histories of τ_3 for the EB, TS, and LS cases with the same assumptions used for the results of Fig. 8, but considering three different tunings for the TS and LS cases, characterized by natural periods of 0.7 s, 1 s, and 1.6 s.

With natural balancing (TS or LS), when the natural period T_n coincides with the vertical motion period T_{vert} (Fig. 9, continuous lines) the actuator torque is very low, and caused only by the unavoidable inertial

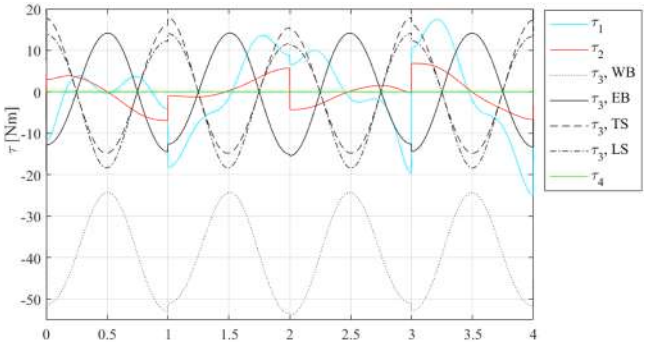

Fig. 8. Actuation torques $\tau_1 \ldots \tau_4$ for the reference trajectory S, T_{vert} =1 s; τ_3 is calculated without balancing (WB), with exact elastic balancing (EB), with natural balancing through a torsional spring (TS) or a linear coil spring (LS); for the TS and LS cases, the elastic elements are tuned with a natural period T_n = 0.7 s.

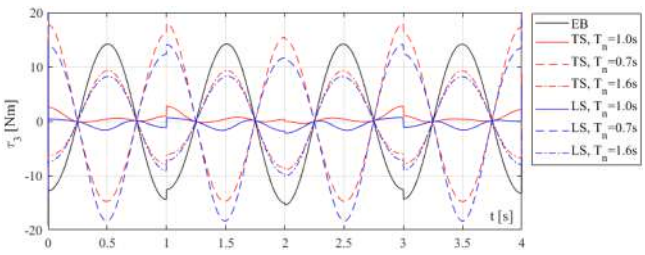

Fig. 9. Comparison of τ_3 with exact balancing (EB), with torsional spring (TS), and with linear coil spring (LS); $T_{vert} = 1$ s, $T_{stop} = 0$ s; three different tunings of the elastic elements are considered for the TS and LS cases, corresponding to T_n = 0.7 s, 1 s, and 1.6 s.

effects related to the horizontal motion. On the other hand, when the elastic elements are too stiff ($T_n < T_{vert}$, dashed lines in Fig. 9) the actuator torque must compensate for the opposition of the elastic elements, which balance gravity inexactly when $\theta_3 \neq 0$; in this condition, the torque oscillations are in counterphase to the EB case. This can be interpreted intuitively, since in the EB case there is no compensation of the inertial forces provided by the elastic elements, while when the elastic elements are too stiff (TS or LS with $T_n < T_{vert}$) this compensation is excessive and changes the sign of the torque with respect to the EB case. On the contrary, when the stiffness of the elastic elements is too low ($T_n > T_{vert}$, dash-dotted lines in Fig. 9), their action is more constant, therefore, the torque oscillations have the same phase of the EB compensation. The fact that, in static conditions, natural balancing is more similar to EB for lower stiffness of the elastic element will be discussed more in depth in Section 9.

7. Influence of the overall robot dynamics on the vertical motion

It is useful to assess the approximation introduced by evaluating the torque τ_3 by the simplified expressions (33) and (37), respectively, in the TS and LS cases, instead of using the complete Eqs. (24) and (28). As discussed in Section 6, the simplified expressions (33) and (37) neglect the inertial effects caused by the overall robot motion on the third actuator, providing an estimation of the vertical natural period. Fig. 10 shows, in continuous lines, torque τ_3 calculated by the complete expressions (24) and (28), which correspond to the multibody simulation results, and in dashed lines, torque τ_3 calculated by the simplified expressions (33) and (37), for the reference motion considered in Section 7, and with the elastic elements tuned to obtain a natural period $T_n = 0.7$ s. It can be observed that the approximation of the simplified expressions is quite accurate, with the maximum differences, as expected, occurring at horizontal direction changes ($t = 0$ s, 1 s, 2 s, 3 s, 4 s), when the inertial effects related to joints J1 and J2, neglected in the simplified expressions of τ_3, are more pronounced.

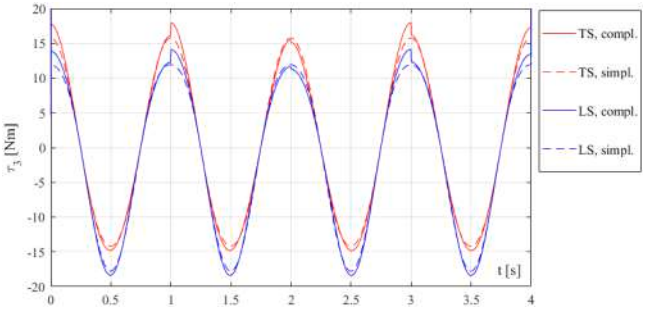

Fig. 10. Comparison of τ_3 calculated in the TS and LS cases using the complete expressions (24) and (28), continuous lines, and the simplified expressions (33) and (37), dashed lines; $T_n = 0.7$ s, T_{vert} =1 s.

8. Influence of finite stop phases on natural and exact elastic balancing

The results reported in Figs. 8–10 are related to a reference motion without finite stop phases. In most applications, the robot stops for small but finite periods, for example, in pick-and-place tasks for grasping or releasing the payload. In the stop phases, there is no power consumption with EB since the robot is statically balanced in any position. On the contrary, with natural balancing, TS or LS, the torque τ_3 and the power consumption are not null in the stop phases if $\theta_3 \neq 0$ since the robot is not statically balanced, and this influences the threshold of convenience between natural and exact balancing.

Fig. 11 shows the same comparison as Fig. 9, with the same reference motion but introducing finite stop phases with duration $T_{stop} = 0.2$ s at the trajectory points A_1, A_2, A_3, and A_4. It is possible to observe that torque τ_3 during the stop phases is not null, and that its constant value depends on the type and stiffness of the elastic elements. The TS balancing determines higher torque in the stop phases than the LS balancing for any natural period T_n. This is because, in the LS case, the elastic return moment is a nonlinear function of θ_3 with a decreasing slope due to the geometry of the mechanical layout shown in Fig. 4; consequently, a lower actuator torque is required to keep the robot stationary with $\theta_3 > 0$ compared to the TS case, where the elastic return moment is linearly proportional to θ_3.

The difference between the TS and LS elastic return moments is shown in Fig. 12, where the two types of elastic return moments are calculated as functions of θ_3 by means of Eqs. (33) and (37) considering only the elastic terms, $\tau_{3el,ts}$ and $\tau_{3el,ls}$. Fig. 12 also shows the gravitational term τ_{3g} as a function of θ_3. Since conditions (34) and (38) are imposed, $\tau_{3el,ts} = \tau_{3el,ls} = \tau_{3g}$ for $\theta_3 = 0$.

Let us note that the difference between $\tau_{3el,ts}$ and τ_{3g} is higher than that between $\tau_{3el,ls}$ and τ_{3g} for $\theta_3 > 0$, for any natural period T_n. On the contrary, for $\theta_3 < 0$, the difference between $\tau_{3el,ts}$ and τ_{3g} is lower than the difference between $\tau_{3el,ls}$ and τ_{3g}. This indicates that the LS balancing is favourable for stop phases with $\theta_3 > 0$, while the TS balancing is favourable for stop phases with $\theta_3 < 0$.

Nevertheless, it should be noted that in practical applications, finite stop phases are often required with $\theta_3 > 0$, typically when the end-effector lowers to operate on the working plane; this is the case simulated with the results shown in Fig. 11. Conversely, finite stop phases with $\theta_3 < 0$ are generally rare, as the end-effector typically rises for the departure, transfer, and approach motions, which should be fast and without stops to minimize the cycle time. This suggests that LS balancing is generally more advantageous than TS balancing in applications involving finite stop phases, which are usually performed with $\theta_3 > 0$.

Regardless of the type of natural balancing, whether TS or LS, the actuator torque during stop phases increases with the stiffness of the elastic elements (corresponding to a lower T_n). In fact, when the elastic elements are stiffer, their return force varies more significantly with θ_3,

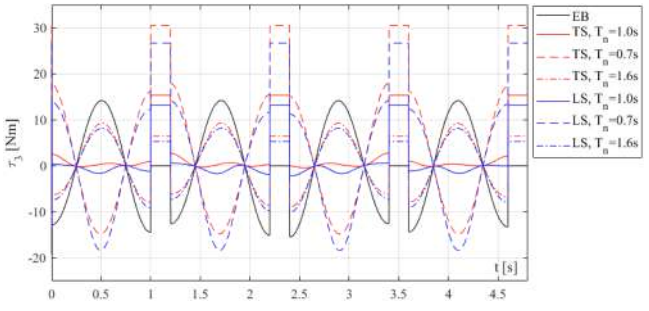

Fig. 11. Comparison of τ_3 with exact balancing (EB), with torsional spring (TS), and with linear coil spring (LS); $T_{vert} = 1$ s, $T_{stop} = 0.2$ s; three different tunings of the elastic elements are considered for the TS and LS cases, corresponding to $T_n = 0.7$ s, 1.0 s, and 1.6 s.

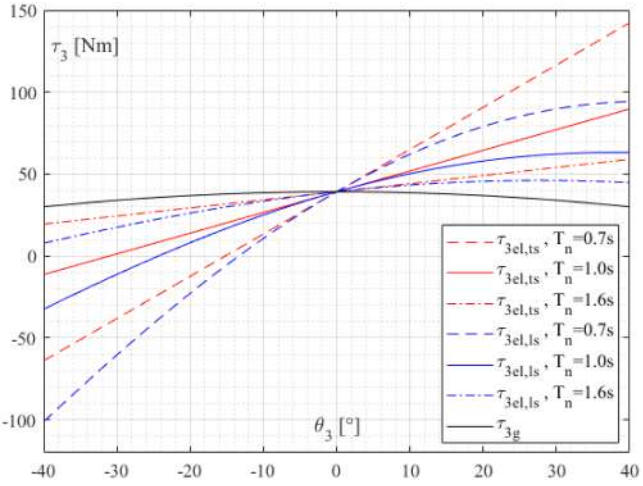

Fig. 12. Elastic moments $\tau_{3el,ts}$ and $\tau_{3el,ls}$ and gravitational moment τ_{3g} as functions of θ_3; three different tunings of the elastic elements are considered, corresponding to $T_n = 0.7$ s, 1.0 s, and 1.6 s.

whereas when they are softer, their effect is more constant and closer to EB, which corresponds exactly to τ_{3g}.

9. Evaluation of the threshold of convenience between natural and exact elastic balancing

The results in the time domain reported in Figs. 9 and 11 show that the threshold of convenience between natural balancing and exact elastic balancing depends on the natural period T_n, the period of the vertical motion T_{vert}, and the stop time T_{stop}. This threshold can be assessed more generally by using two global performance indexes: the maximum absolute value of the torque τ_3 ($\tau_{3,max}$), and the Integral Control Effort (*ICE*) calculated as follows:

$$ICE = \sum_{i=1}^{4} \int_0^{T_{mot}} \sigma_i(t)\tau_i^2(t)dt, \sigma_i(t) = \begin{cases} 1 \text{ if } P_i \geq 0 \\ 0 \text{ if } P_i < 0 \end{cases} \quad (48)$$

In Eq. (48), T_{mot} represents the overall motion time, and P_i denotes the mechanical power of the i th actuator, calculated as the product of its torque and angular velocity. In the time integral, the variable $\sigma_i(t)$ is introduced to account for energy consumption only during phases where the mechanical power is positive, i.e., when torque and angular velocity have the same sign, or zero, in stop phases with non-null torque. As a matter of fact, modern electrical drivers typically brake, delivering negative mechanical power, without electrical power consumption. Depending on the capabilities of the electronic driver, the negative power can be dissipated as heat through a resistor, stored in a capacitor, or even transferred back to the energy source in the case of regenerative drivers with active front end [26]. For an accurate estimation of power consumption, detailed knowledge of the functional schemes and parameters of both the electrical motor and the electronic drivers is necessary. Comprehensive models of the power flow in servo-actuated mechatronic and robotic systems have been proposed in the scientific literature [27–30]. However, the objective of this research is to assess power consumption independently of the specific choice of actuators and drivers, focusing on the benefits of exploiting natural motion. The adoption of regenerative drivers, combined with direct-drive rotary actuators, such as in the proposed SCARA-like architecture, can further reduce the robot's power consumption, with the extent of reduction depending on the efficiency of electrical regeneration. In this study, power consumption is estimated using the *ICE* defined in Eq. (48), which provides the significant advantage of being independent of the specific electrical and electronic architecture and its parameters. This approach focuses on the energy savings achieved through mechanical design

rather than those resulting from the electronic driver design. Naturally, these two complementary approaches can be combined in the final robot design to maximize overall efficiency.

For natural balancing, TS and LS, a two-dimensional matrix of multibody simulations has been performed varying the natural period T_n and the vertical motion period T_{vert}, adopting the same robot geometrical and inertial parameters used for the simulations reported in Sections 6, 7 and 8. As discussed in Section 6, for a given value of T_n all the parameters of the elastic elements are fully defined by conditions (41), (46), and (47).

In order to assess the influence of different types of horizontal motions, the matrix of simulations has been performed not only for the square reference trajectory S (Fig. 7), but also for the trajectory R (Fig. 13).

This trajectory is characterized by the same harmonic vertical motion with range $h_t = 0.2$ m and period T_{vert}, but with 12 horizontal movements CB_iC, with period $2T_{vert}$ and amplitude $d_t = 0.2$ m, starting from C and with 12 equally spaced radial directions in the horizontal plane (Fig. 13, b). Similarly to the S trajectory, it is easy to demonstrate that, since the horizontal motion period is double the vertical motion period, the elementary movements CB_iC are characterized by parabolic trajectories lying in vertical planes (Fig. 13, a).

Moreover, to evaluate the influence of stop phase (Section 8), two conditions are considered for both the S and R trajectories: no stop phase between the elementary movements ($T_{stop} = 0$ s), and stop phases with duration $T_{stop} = 0.2T_{vert}$ at the end of each elementary movement (A_iA_{i+1} for the S trajectory, and CB_iC for the R trajectory).

The 3D graphs of Figs. 14, 15, 16, and 17 show the two global performance indexes, $\tau_{3,max}$ and ICE, as functions of T_n and T_{vert}, both ranging from 0.4 s to 2.2 s. These figures represent the four combinations resulting from the two trajectories and the presence or absence of stop phases. In these 3D graphs, the values of the global performance indexes are expressed as a percentage relative to the same indexes calculated without balancing. The red and blue surfaces refer to natural balancing respectively in the TS and LS cases; the green surfaces are relative to the EB case and do not depend on T_n, since the tuning of the elastic element for EB is constant.

From the observation of the 3D graphs of Figs. 14–17, it is possible to outline the following conclusions:

- as expected, with natural balancing, both the performance indexes have local minima, for any value of the motion time T_{vert}, very close to the resonance condition $T_n = T_{vert}$;
- for $T_{vert} >> T_n$ (commanded motions significantly slower than the natural motion), EB outperforms natural balancing (TS or LS); conversely, for $T_{vert} << T_n$ (commanded motions significantly faster

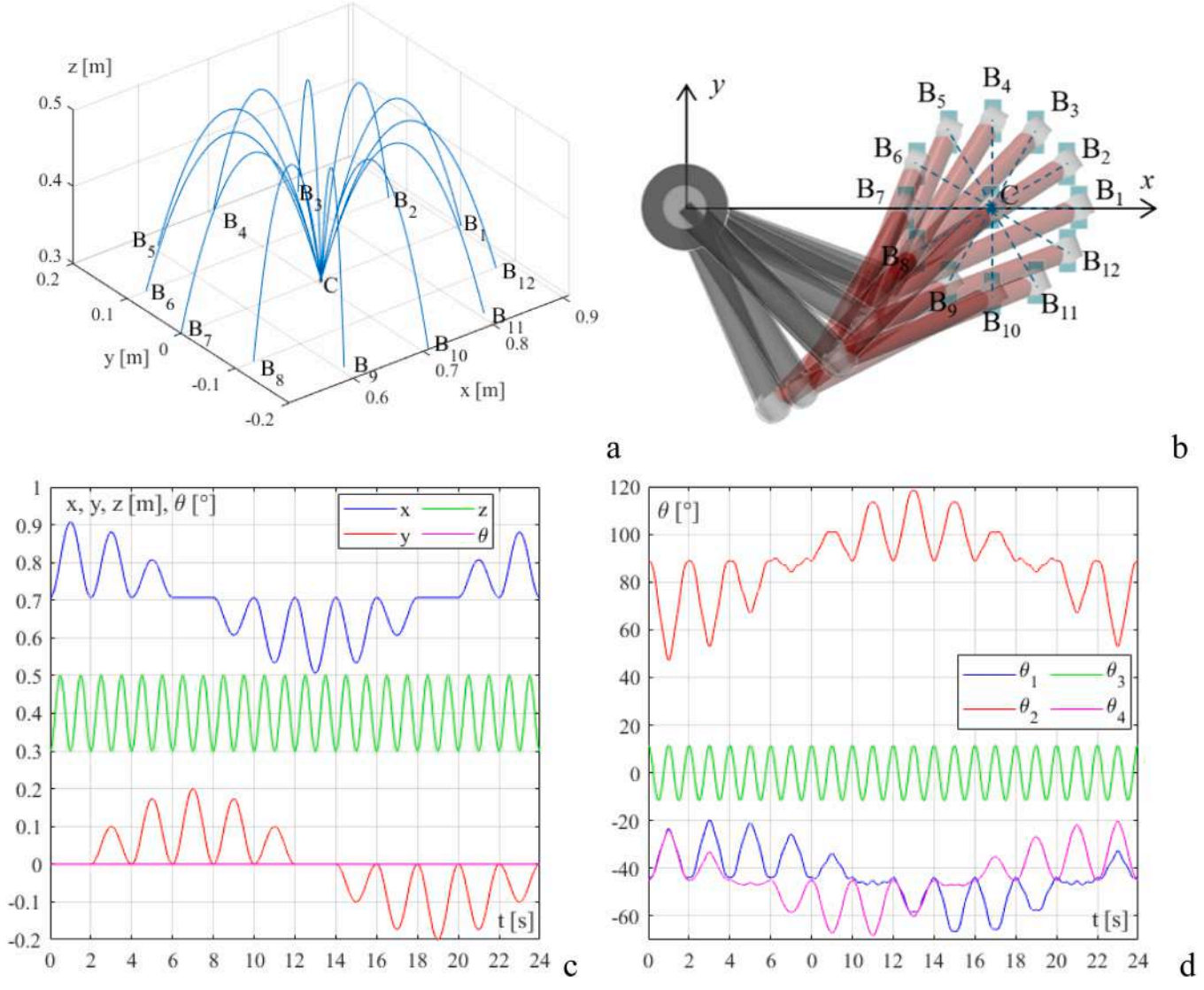

Fig. 13. Radial reference trajectory R (a, b), with the corresponding external and internal coordinates (c, d), $T_{vert} = 1$ s.

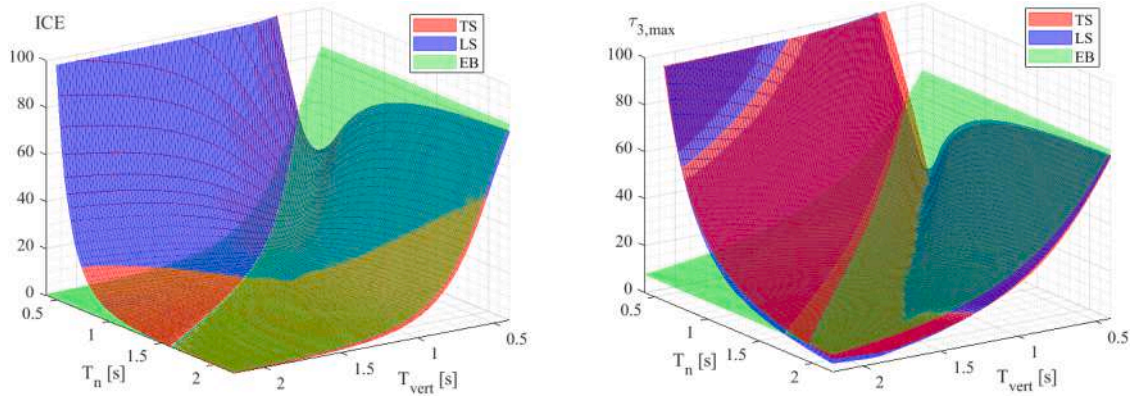

Fig. 14. *ICE* and $\tau_{3,\max}$ as functions of T_{vert} and T_n, trajectory *S*, $T_{stop} = 0$ s (percentage ratios w.r.t. WB).

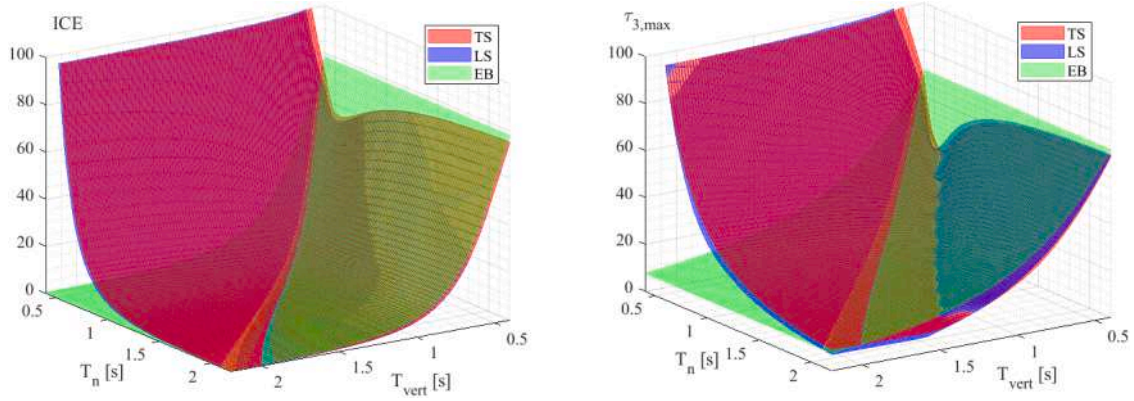

Fig. 15. *ICE* and $\tau_{3,\max}$ as functions of T_{vert} and T_n, trajectory *S*, $T_{stop} = 0.2 \cdot T_{vert}$ (percentage ratios w.r.t. WB).

than the natural motion), natural motion is more advantageous compared to EB;

- the thresholds of convenience between TS and EB, as well as between LS and EB, are represented in Fig. 18 for the four considered combinations of Figs. 14–17; all these thresholds are lines in the (T_n, T_{vert}) plane located close to the resonance condition $T_{vert} = T_n$, but with some differences;
- the *ICE* thresholds (Fig. 18, left) are nearly identical for both trajectories and both types of natural balancing in the absence of stop phases; conversely, in the presence of stop phases, the *ICE* thresholds become more distinct; in general, the presence of finite stop phases expands the region where EB is more advantageous, for the reasons discussed in Section 8; this effect is more pronounced for the *S* trajectory, where a stop phase occurs after each vertical motion, whereas in the *R* trajectory a stop phase occurs after a pair of vertical motions; furthermore, as explained in Section 8, LS balancing is preferable to TS in the presence of stop phases with $\theta_3 > 0$, resulting in a wider region of convenience for LS compared to TS;
- the $\tau_{3,\max}$ thresholds (Fig. 18, right) are similar to those of the *ICE*: also for this performance index, in the presence of finite stop phases, the region of convenience of EB is wider, and LS is preferable to TS; for $\tau_{3,\max}$, the influence of the trajectory type is null in the absence of stop phases (the thresholds are coincident) or very limited in the presence of finite stop phases, since this performance index is a maximum value and not a time integral along the whole motion;

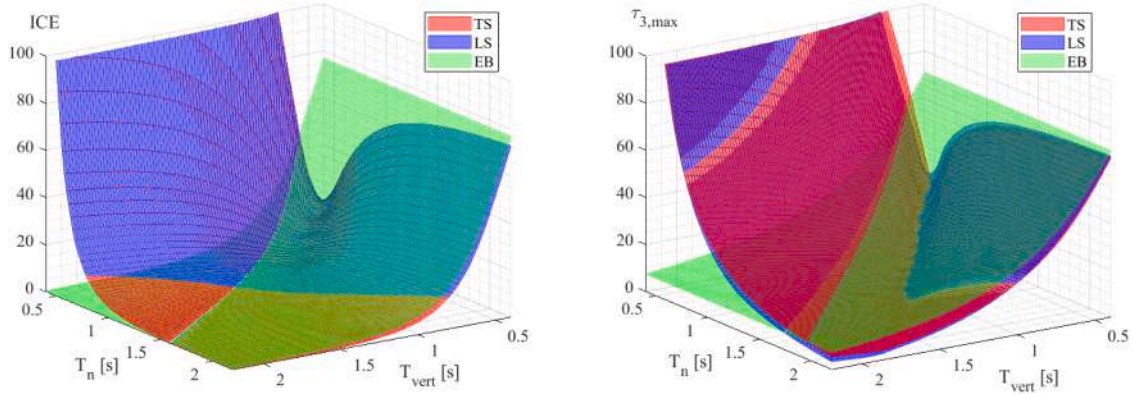

Fig. 16. *ICE* and $\tau_{3,\max}$ as functions of T_{vert} and T_n, trajectory *R*, $T_{stop} = 0$ s (percentage ratios w.r.t. WB).

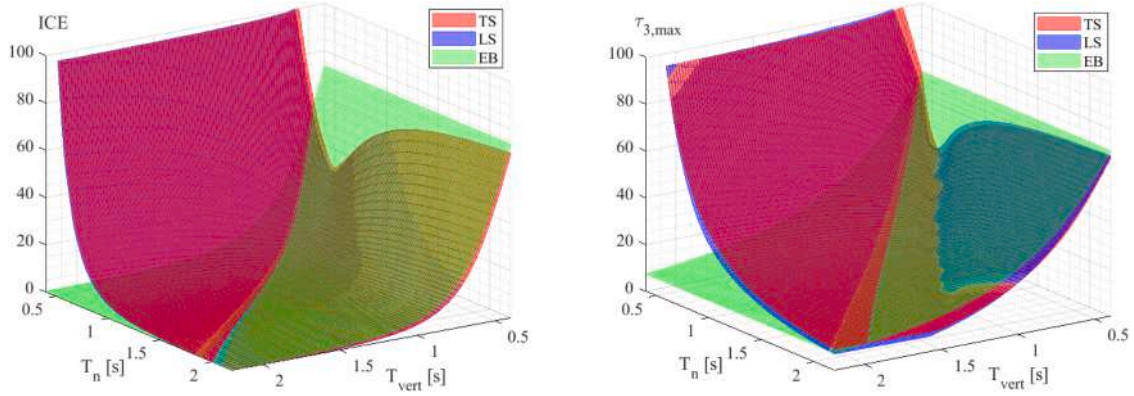

Fig. 17. *ICE* and $\tau_{3,\max}$ as functions of T_{vert} and T_n, trajectory *R*, $T_{stop} = 0.2 \cdot T_{vert}$ (percentage ratios w.r.t. WB).

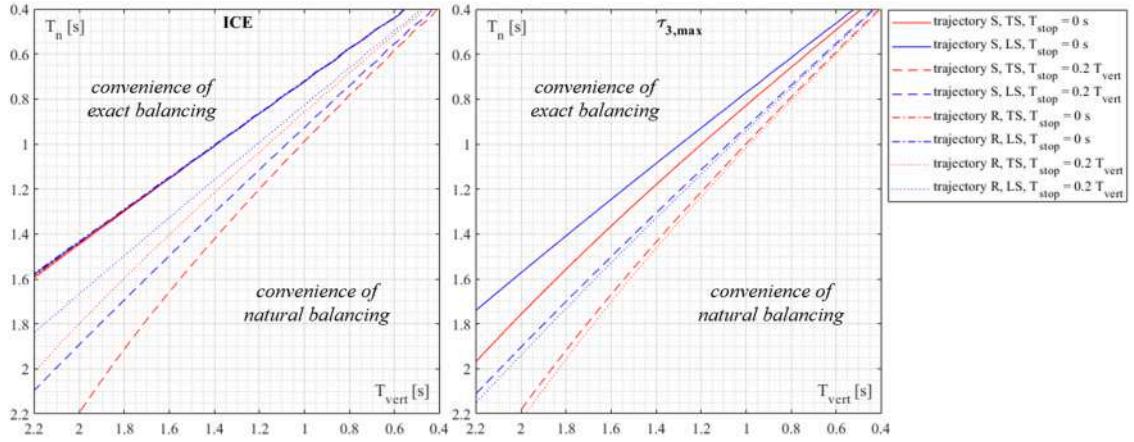

Fig. 18. Thresholds of convenience between TS and EB (red) and between LS and EB (blue) for *ICE* (left) and $\tau_{3,\max}$ (right).

- observing Figs. 14 and 16, it is possible to note that in the absence of finite stop phases, the differences between TS and LS are, in general, limited both for the *ICE* and for $\tau_{3,\max}$; as regards the *ICE*, TS is slightly advantageous in the zones of the (T_n, T_{vert}) plane with low T_{vert} and T_n, while LS is slightly convenient for faster motions and stiffer tunings of the elastic elements; as regards $\tau_{3,\max}$, LS is in general slightly advantageous over TS in a wide region across the resonance condition; conversely, observing Figs. 15 and 17, it is evident that LS outperforms TS in almost all the (T_n, T_{vert}) plane.

The benefits of natural balancing are maximum in the resonance condition ($T_n = T_{vert}$). The graphs of Fig. 19 represent the differences of *ICE* (left) and $\tau_{3,\max}$ (right) between TS and EB (red) and between LS and EB (blue), expressed in percentage ratios with respect to the WB case, in the resonance condition. These graphs are obtained by the sections of the 3D surfaces of Figs. 14–17 along the vertical plane $T_n = T_{vert}$.

It is possible to observe that, for both the performance indexes, the benefits of natural motion are higher for fast motions, as expected, since inertial forces become predominant. For $T_{vert} = 0.4$ s, the *ICE* reduction ranges from about −51 % for trajectory *R* without stop phases, both for

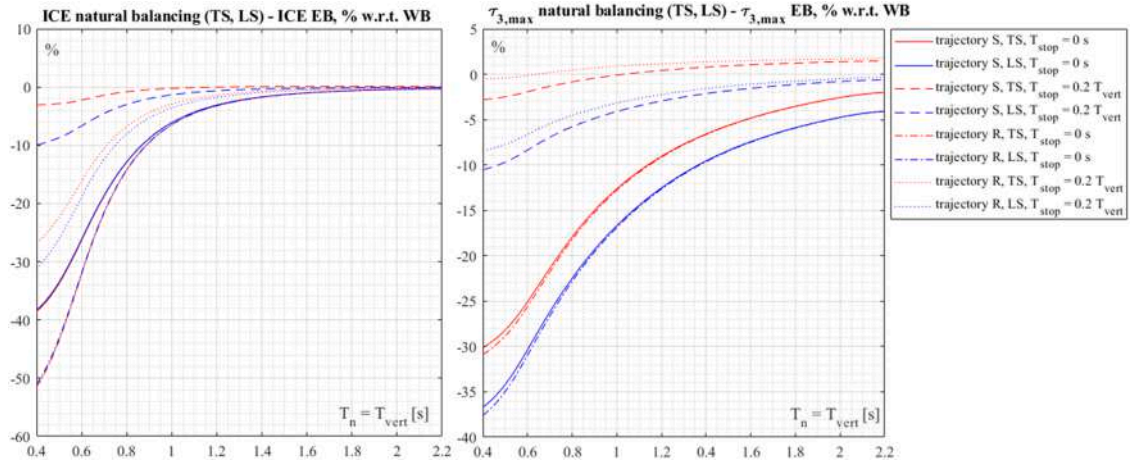

Fig. 19. Difference of *ICE* (left) and $\tau_{3,\max}$ (right) between TS and EB (red) and between LS and EB (blue), expressed in percentage ratios w.r.t. WB.

TS and LS balancing, to about −3 % for trajectory *S* with stop phases. As the motion time increases, the *ICE* of natural balancing and of exact balancing tend to be equal. Also, the proficiency in terms of $\tau_{3,\max}$ is maximum for the lowest value of motion time, ranging from about −37 % for LS without stop phases to about −0.5 % for trajectory *R* with stop phases. It is interesting to note that as the motion time increases, in the presence of stop phases, $\tau_{3,\max}$ can be higher with TS balancing than with EB, while LS balancing always outperforms EB in resonance conditions, independently of the motion time and of the presence of stop phases. This represents another advantage of LS balancing over TS balancing.

10. Possible strategies for tuning in the presence of variable payload mass

The results discussed in Sections 6, 7, 8, and 9 have been obtained considering a constant payload mass. Nevertheless, in many practical situations, the payload varies during the task. For example, in pick-and-place operations, the payload can be present or absent depending on the considered phase, or there can be different payload masses, sometimes not known a priori.

Even if the payload mass is smaller than that of the robot links, its influence on the equivalent inertia of the four-bar moving in a vertical plane, expressed by Eq. (17), is not negligible, since m_6 (sum of the end-effector mass m_{ee} and the payload mass m_p) is multiplied by l_3^2. Consequently, the influence of the payload mass on the vertical natural period T_n is not negligible, as estimated at the end of Section 5 (Fig. 6).

In the case of payload variation, different alternative approaches can be followed. The simplest approach is to adopt a vertical motion period T_{vert} intermediate between the minimum natural period without payload ($T_{n,0}$) and the natural period with the considered payload ($T_{n,1}$).

For example, let us consider the case study of Fig. 9, related to the reference trajectory *S*, composed of four elementary movements A_iA_{i+1}. In this case study, a constant payload mass $m_p = 0.5$ kg is imposed. Now, instead, let us suppose that the first and third phases of the reference motion, A_1A_2 and A_3A_4, are performed without payload, while the second and fourth phases, A_2A_3 and A_4A_1, are performed with a payload of 1 kg. This occurs if the gripper instantaneously grasps the payload in A_2 and A_4, and instantaneously releases the payload in A_3 and A_1. This is theoretically feasible since the reference trajectory has null velocity for the *x, y, z* coordinates at the points A_i, as it can be observed by the *x, y, z* time-histories in Fig. 7, c. Finite stop phases can be introduced for a more reliable grasp and release, with the effects discussed in Section 8. However, in the following, we will not consider finite stop phases to focus only on the influence of the payload variation.

Using the procedure discussed in Section 6, considering the same robot parameters of the case study of Fig. 9 but imposing a natural period $T_{n,1} = 1.0$ s with a payload of 1 kg, the following parameters of the elastic elements are obtained: $k_{ts} = 77.31$ Nm/rad, $\theta_{3n} = -0.5393$ rad, $k_{ls} = 1081.4$ N/m, $l_{und} = 0.2880$ m. With these parameters, in the absence of the payload, the natural period reduces to $T_{n,0} = 0.9340$ s. Fig. 20, a shows the simulation results for torque τ_3 in the EB, TS and LS cases, adopting a vertical motion period $T_{vert} = 0.9670$ s, average between $T_{n,0}$ and $T_{n,1}$. The overall cycle time is 3.868 s.

It is possible to note that natural balancing (both TS and LS) is still more efficient than EB in overcoming the inertial forces, since it provides a significant reduction of the peak torque (–49.3 % for TS and –62.7 % for LS compared to EB), even if the tuning of the vertical motion period and natural period is a compromise between the presence or absence of the payload. This confirms the results discussed in Section 9, which show that the region of convenience of natural balancing is quite wide, and not strictly limited to the resonance condition.

Observing Fig. 20, a, it is possible to see that the torque peaks for EB, related to the inertial forces, are higher in the second and fourth phases, when the payload is present. Moreover, it is interesting to note that, since the elastic elements are tuned considering the payload, the torque with natural balancing, TS or LS, is close to zero in the second and fourth phases, when the payload is present. On the contrary, the TS and LS torques are always positive in the first and third phases, since the balancing of gravitational forces is not exact without payload. It is possible to optimize the tuning of the elastic elements for the specific task; otherwise, a good compromise is to tune the elastic elements considering an intermediate payload.

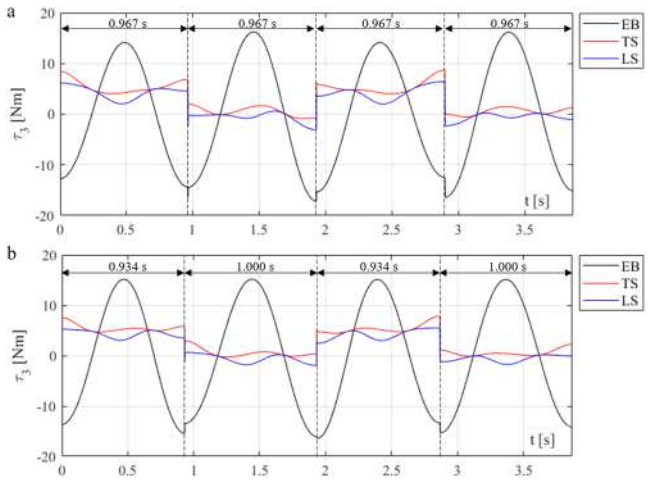

Fig. 20. Trajectory *S*, variable payload ($m_p = 0$ kg for the A_1A_2 and A_3A_4 phases, $m_p = 1$ kg for the A_2A_3 and A_4A_1 phases); comparison of τ_3 with exact balancing (EB), with torsional spring (TS), and with linear coil spring (LS); $T_{vert} = 0.9670$ s for all the phases (a); $T_{vert} = 0.9340$ s for the A_1A_2 and A_3A_4 phases, and $T_{vert} = 1$ s for the A_2A_3 and A_4A_1 phases (b).

Another possible approach to face payload variations is to change the vertical motion period according to the payload. For example, it is possible to impose $T_{vert} = T_{n,0}$ for the first and third phases, and $T_{vert} = T_{n,1}$ for the second and fourth phases. The results of this tuning approach are represented in Fig. 20, b.

Adopting this reference trajectory with variable vertical motion period, the torque peaks with EB are almost equal in all the phases, since the presence of the payload is compensated by a slower motion. It is interesting to observe that this tuning approach outperforms the previous one, with constant vertical motion period, since it achieves a higher torque reduction compared to EB (–52.6 % for TS and –66.6 % for LS) with the same overall cycle time. This highlights the importance of following as much as possible the natural oscillations of the mechanical architecture.

11. Conclusions

Starting from the kinematic and dynamic models of the SCARA-like RR-4R-R manipulator, the effectiveness of different types of elastic balancing has been compared. The first comparison is between exact elastic balancing, which provides indifferent equilibrium in any position without giving rise to natural motion, and natural balancing, which originates natural motion, exploitable for cyclic movements. Moreover, two types of natural balancing have been examined: through a torsional spring with linear characteristic, and through a linear coil spring. Based on the dynamic model, the relationships to tune the elastic elements for a desired natural period T_n in the torsional spring and linear coil spring cases have been obtained and used to perform matrices of multibody simulations in the (T_n, T_{vert}) space. These matrices of simulations have been run considering different trajectories, and in the presence or absence of finite stop phases. Simulation results indicate that, even if the natural balancing is applied only to the actuator that drives the vertical motion, the energy consumption reduction is significant, with a decrease of the integral control effort up to −51 %, and a decrease of the maximum actuation torque up to −37 % for the considered geometrical and inertial parameters of the manipulator. Moreover, the simulation

results indicate that balancing through a linear coil spring provides better performance, especially in the presence of stop phases, in addition to being much easier to implement from a construction standpoint. In conclusion, these results pave the way for the development of a new family of 4-degree-of-freedom manipulators, significantly reducing the carbon footprint in all robotic production lines where SCARA robots are currently employed. In general, the development of innovative mechanical architectures, even bio-inspired ones [31], that include elastic elements and exploit their natural motion can lead to significant functional and energy benefits not only in the field of industrial robotics but also in service and assistive robotics [32].

CRediT authorship contribution statement

Luca Bruzzone: Writing – original draft, Validation, Software, Methodology, Investigation, Formal analysis, Conceptualization. **Matteo Verotti:** Writing – review & editing, Validation, Software. **Pietro Fanghella:** Writing – review & editing, Supervision, Project administration.

Declaration of competing interest

The authors declare that they have no known competing financial interests or personal relationships that could have appeared to influence the work reported in this paper.

Data availability

Data will be made available on request.

References

[1] C. Xu, H.L. Zhang, B. Lin, Achieving pollution abatement and carbon reduction synergistically: how can industrial robots play a role? J. Environ. Manag. 373 (2025) 123816 https://doi.org/10.1016/j.jenvman.2024.123816.

[2] M. Yao, X. Zhou, Z. Shao, L. Wang, A general energy modeling network for serial industrial robots integrating physical mechanism priors, Robot. Comput. Integr. Manuf. 89 (2024) 102761, https://doi.org/10.1016/j.rcim.2024.102761.

[3] C. Müller, World Robotics 2024 – Industrial Robots, IFR Statistical Department, VDMA Services GmbH, Frankfurt Am. Main, Germany, 2024.

[4] G. Carabin, E. Wehrle, R. Vidoni, A review on energy-saving optimization methods for robotic and automatic systems, Robotics 6 (4) (2017) 39, https://doi.org/10.3390/robotics6040039.

[5] A. Albu-Schäffer, S. Haddadin, C. Ott, A. Stemmer, T. Wimböck, G. Hirzinger, The DLR lightweight robot: design and control concepts for robots in human environments, Ind. Robot. 34 (2007) 376–385, https://doi.org/10.1108/01439910710774386.

[6] P. Boscariol, P. Gallina, A. Gasparetto, M. Giovagnoni, L. Scalera, R. Vidoni, Evolution of a dynamic model for flexible multibody systems. Advances in Italian Mechanism Science, Springer, Berlin, Germany, 2017, pp. 533–541, https://doi.org/10.1007/978-3-319-48375-7_57.

[7] J. Heredia, R.J. Kirschner, C. Schlette, S. Abdolshah, S. Haddadin, M.B. Kjaegaard, ECDP: energy consumption disaggregation pipeline for energy optimization in lightweight robots, IEEE Robot. Autom. Lett. 8 (10) (2023) 6107–6114, https://doi.org/10.1109/LRA.2023.3301311.

[8] G. Lee, S. Park, D. Lee, F.C. Park, J.I. Jeong, J. Kim, Minimizing energy consumption of parallel mechanisms via redundant actuation, IEEE/ASME Trans. Mechatron. 20 (6) (2015) 2805–2812, https://doi.org/10.1109/TMECH.2015.2401606, 7217819.

[9] D. Margolis, Energy regenerative actuator for motion control with application to fluid power systems, J. Dyn. Syst. Meas. Control Trans. ASME 127 (1) (2005) 33–40, https://doi.org/10.1115/1.1870038.

[10] Z. Yang, J. Sun, Y. Tang, M. Huang, X. Zha, An integrated dual voltage loop control for capacitance reduction in CHB-based regenerative motor drive systems, IEEE Trans. Ind. Electron. 66 (5) (2019) 3369–3379, https://doi.org/10.1109/TIE.2018.2854606, 8411432.

[11] Z. Liu, Y. Huang, D. Liu, X. Guo, K. Wang, J. Tan, Trajectory planning of large redundant manipulator considering kinematic constraints and energy efficiency, Robotica 41 (11) (2023) 3524–3540, https://doi.org/10.1017/S0263574723001157.

[12] G. Trigatti, P. Boscariol, L. Scalera, D. Pillan, A. Gasparetto, A new path-constrained trajectory planning strategy for spray painting robots-rev, Int. J. Adv. Manuf. Technol. 98 (2018) 2287–2296, https://doi.org/10.1007/s00170-018-2382-2.

[13] G. Carabin, L. Scalera, On the trajectory planning for energy efficiency in industrial robotic systems, Robotics 9 (4) (2020) 1–13, https://doi.org/10.3390/robotics9040089, 89.

[14] L. Scalera, I. Palomba, E. Wehrle, A. Gasparetto, R. Vidoni, Natural motion for energy saving in robotic and mechatronic systems, Appl. Sci. 9 (17) (2019) 3516, https://doi.org/10.3390/app9173516.

[15] E. Bolívar, S. Rezazadeh, R. Gregg, Minimizing energy consumption and peak power of series elastic actuators: a convex optimization framework for elastic element design, IEEE/ASME Trans. Mechatron. 23 (2019) 1334–1345, https://doi.org/10.1109/TMECH.2019.2906887.

[16] M. Iwamura, W. Schiehlen, Minimum control energy in multibody systems using gravity and springs, J. Syst. Des. Dyn. 5 (2011) 474–485, https://doi.org/10.1299/jsdd.5.474.

[17] R. Nasiri, M. Khoramshahi, M. Shushtari, M.N. Ahmadabadi, Adaptation in variable parallel compliance: towards energy efficiency in cyclic tasks, IEEE/ASME Trans. Mechatron. 22 (2017) 1059–1070, https://doi.org/10.1109/TMECH.2016.2637826.

[18] R. Jimenez-Fabian, M. Weckx, D. Rodriguez-Cianca, D. Lefeber, B. Vanderborght, Online reconfiguration of a variable-stiffness actuator, IEEE/ASME Trans. Mechatron. 23 (2018) 1866–1876, https://doi.org/10.1109/TMECH.2018.2841193.

[19] J.P. Mora, J.P. Barreto, C.F. Rodriguez, Energy optimization of a parallel robot in pick and place tasks, Mech. Mach. Sci. 110 MMS (2022) 191–200, https://doi.org/10.1007/978-3-030-88751-3_20.

[20] L. Righetti, J. Buchli, A.J. Ijspeert, Adaptive frequency oscillators and applications, Open Cybern. Syst. J. 3 (1) (2009) 64–69, https://doi.org/10.2174/1874110X00903020064.

[21] L. Bruzzone, G. Bozzini, A statically balanced SCARA-like industrial manipulator with high energetic efficiency, Meccanica 46 (4) (2011) 771–784, https://doi.org/10.1007/s11012-010-9336-6.

[22] L. Bruzzone, M. Verotti, P. Fanghella, Natural motion of the RR-4R-R manipulator: effects of trajectory types and parameters, Mech. Mach. Sci. 179 (2025) 238–245, https://doi.org/10.1007/978-3-031-91151-4_27.

[23] H. Goya, K. Matsusaka, M. Uemura, Y. Nishioka, S. Kawamura, Realization of high-energy efficient pick-and-place tasks of SCARA robots by resonance, in: Proceedings of the IEEE/RSJ International Conference on Intelligent Robots and Systems (IROS), Vilamoura, Portugal, 2012, pp. 2730–2735, https://doi.org/10.1109/IROS.2012.6386084, 7–12 October.

[24] G. Lu, S. Kawamura, M. Uemura, Proposal of an energy saving control method for SCARA robots, J. Robot. Mechatron. 24 (1) (2012) 115–122, https://doi.org/10.20965/jrm.2012.p0115.

[25] D. Franchetti, G. Boschetti, B. Lenzo, Passive gravity balancing with a self-regulating mechanism for variable payload, Machines 9 (2021) 145, https://doi.org/10.3390/machines9080145.

[26] A. Hughes, Electric Motors and Drives Fundamentals. Types and Applications, 3rd ed., Elsevier, London, 2006.

[27] E. Oliva, G. Berselli, M. Pellicciari, A. Andrisano, An engineering method for the power flow assessment in servo-actuated automated machinery: mechatronic modeling and experimental evaluation, Robot. Comput. Integr. Manuf. 38 (2016) 31–41, https://doi.org/10.1016/j.rcim.2015.09.013.

[28] G. Berselli, F. Balugani, M. Pellicciari, M. Gadaleta, Energy-optimal motions for servo-systems: a comparison of spline interpolants and performance indexes using a CAD-based approach, Robot. Comput. Integr. Manuf. 40 (2016) 55–65, https://doi.org/10.1016/j.rcim.2016.01.003.

[29] Z. Wang, X. Li, P. Jiang, X.V. Wang, H. Yuan, Energy consumption modeling based on operation mechanisms of industrial robots, Robot. Comput. Integr. Manuf. 94 (2025) 102971, https://doi.org/10.1016/j.rcim.2025.102971.

[30] P. Boscariol, D. Richiedei, Energy-efficient design of multipoint trajectories for cartesian robots, Int. J. Adv. Manuf. Technol. 102 (2019) 1853–1870, https://doi.org/10.1007/s00170-018-03234-4.

[31] A.S. Robbins, M. Ho, M. Teodorescu, Model-free dynamic control of robotic joints with integrated elastic ligaments, Rob. Aut. Syst. 155 (2022) 104150, https://doi.org/10.1016/j.robot.2022.104150.

[32] N. Zhou, Y. Liu, Song, Qiuzhi Zhuo Qi, Weizhi Ren, Kun Zhang, Analysis, design and preliminary evaluation of an anthropometric self-stabilization passive exoskeleton for enhancing the ability of walking with loads, Rob. Aut. Syst. 153 (2022) 104079, https://doi.org/10.1016/j.robot.2022.104079.